Cold Regions Science and Technology 253 (2027) 105164

Contents lists available at ScienceDirect

Cold Regions Science and Technology

journal homepage: www.elsevier.com/locate/coldregions

Mesoscale numerical modelling of freeze–thaw deformation in closed- and open-system soils using a Voronoi–Delaunay lattice

Zarghaam Rizvi [a,b,*], Mohammad Arsalan Khan [b,c], Frank Wuttke [b]

[a] Department of Civil and Environmental Engineering, University of Waterloo, Waterloo, Ontario, Canada
[b] Geomechanics and Geotechnics Group, Kiel University, 24118 Kiel, Germany
[c] Department of Civil Engineering, Z. H. College of Engineering and Technology, Aligarh Muslim University, Aligarh, India

ARTICLE INFO

Keywords:
Frozen soil
Frost heave
Thaw settlement
Lattice element method
Voronoi–Delaunay mesh
Thermo-hydro-mechanical model

ABSTRACT

Freeze–thaw deformation in frost-susceptible soils couples heat transfer, phase change, water redistribution and irreversible thaw deformation. This study develops an axisymmetric Voronoi–Delaunay lattice framework with a finite-element-analysis-program (FEAP)-compatible residual–tangent organization, embedded displacement-jump histories and a bounded temperature-dependent creep law. Delaunay edges carry normal–shear interactions, while a circumcentric dual supplies transport faces and storage volumes. The global benchmark implementation combines apparent-heat-capacity heat transfer, a reduced total-water redistribution equation and fixed-reference small-strain lattice mechanics; it is not a complete Darcy-flow, effective-stress or discrete ice-lens formulation. Verification against radial conduction, Stefan-front propagation and confined compression produced errors of 1.45%, 3.53% and 5.88%, respectively. First-cycle heave and thaw-settlement endpoints from one closed Kieler Förde test and six independent open-system tests were used for case-level calibration. The calibrated model reproduced those endpoints with a median absolute percentage error of 0.36%. The subsequent Kieler Förde cycle trend was assessed without further endpoint calibration, and the FEAP jump–creep enrichment retained a median endpoint error of 3.03% without re-optimisation. Predicted temperature, ice fraction, total water, pressure proxy and displacement fields are reported as model outputs because co-registered water-content profiles, pore pressures and freezing-front positions were not available for every case. Four CPU workers produced a measured 3.25-fold batch speedup; an optional GPU sparse-solver route is supplied with deterministic CPU fallback. The framework is therefore intended for rapid laboratory-scale displacement assessment, while finite-strain kinematics and fully coupled ice-lens poromechanics remain future developments.

1. Introduction

Frozen and seasonally frozen soils are multiphase geomaterials in which conductive heat transfer, latent heat, unfrozen-water migration, ice formation, cryogenic suction, stress redistribution and fabric change evolve on comparable time scales. Pore-water freezing alone produces a finite volumetric expansion, whereas sustained segregation heave requires a frost-susceptible fabric, a thermal gradient and access to mobile water; thawing removes ice cementation and can generate excess pore water, consolidation and irreversible rearrangement (Taber, 1930; Miller, 1972; Konrad and Morgenstern, 1981; O'Neill and Miller, 1985; Andersland and Ladanyi, 2004; Rempel, 2007; Morgenstern and Nixon, 1971). Consequently, the measured response depends on particle-size distribution, mineralogy, plasticity, initial density, stress history, hydraulic conductivity, degree of saturation, salinity, drainage condition, freezing rate and cycle history (Chamberlain and Gow, 1979; Chamberlain, 1981; Konrad, 1989; Viklander, 1998; Benson and Othman, 1993; Konrad and Lemieux, 2005; Wang et al., 2007; Eigenbrod, 1996; Eigenbrod et al., 1996; Wong and Haug, 1991; Hendry et al., 2016). A numerical method intended for laboratory assessment must therefore represent the imposed thermal and hydraulic boundaries explicitly and must separate reversible phase deformation from irreversible cyclic settlement.

Analytical and semi-analytical models remain indispensable because they establish governing scales and provide controlled verification targets. Fourier-series solutions describe transient heat conduction in slabs and cylinders, Stefan and Neumann solutions relate phase-front position to thermal diffusivity and latent heat, and segregation-potential or rigid-

* Corresponding author at: Department of Civil and Environmental Engineering, University of Waterloo, Waterloo, Ontario, Canada.
E-mail address: zarghaam.rizvi@ifg.uni-kiel.de (Z. Rizvi).

https://doi.org/10.1016/j.coldregions.2026.105164
Received 1 August 2026; Received in revised form 3 September 2026; Accepted 15 September 2026
Available online 6 October 2026
0165-232X/© 2026 The Authors. Published by Elsevier B.V. This is an open access article under the CC BY license (http://creativecommons.org/licenses/by/4.0/).
Open access funding enabled and organized by Projekt DEAL.

ice formulations relate heave rate to the frozen-fringe thermal gradient and water supply (Stefan, 1891; Carslaw and Jaeger, 1959; Crank, 1984; Konrad and Morgenstern, 1981; Konrad and Seto, 1994; O'Neill and Miller, 1985; Gilpin, 1980). Coupled heat and moisture models derived from energy conservation, Darcy-type transport, the Clapeyron relation and soil-freezing characteristic curves provide additional physical structure (Harlan, 1973; Koopmans and Miller, 1966; Spaans and Baker, 1996; van Genuchten, 1980; Fredlund and Xing, 1994; Dall'Amico, 2011). Their efficiency and interpretability make them suitable for code verification, but closed-form solutions normally require regular geometry, homogeneous properties, simplified interfaces and restricted mechanical coupling. They cannot, by themselves, reproduce both an externally cooled closed oedometer and an open top-down column with evolving water redistribution and path-dependent deformation.

Continuum numerical methods have accordingly dominated frozen-soil analysis. Finite-element formulations have coupled energy, water mass, poromechanics, effective stress, elastic or elastoplastic response, ice segregation and thaw consolidation in one, two and three dimensions (Nishimura et al., 2009; Thomas et al., 2009; Zhang and Michalowski, 2015; Zhelnin et al., 2022; Liu et al., 2024; Norouzi and Li, 2024). Finite-difference and finite-volume schemes remain attractive for structured transport problems because flux conservation and transient storage are direct (Harlan, 1973; Patankar, 1980; Wu et al., 2021). Boundary-element methods reduce the dimensionality of suitable linear homogeneous problems, but internal phase change, heterogeneous coefficients and distributed state variables weaken this advantage (Brebbia et al., 1984). Biot-type poromechanics, retention relationships and freezing characteristic curves provide a rigorous continuum basis for coupled stress and water transport (Biot, 1941; van Genuchten, 1980; Fredlund and Xing, 1994; Koopmans and Miller, 1966; Spaans and Baker, 1996). Nevertheless, nonlinear constitutive updates, moving phase transitions, discontinuities, repeated cycles and large-deformation stabilisation can increase implementation and computational cost.

Discrete and hybrid methods resolve complementary aspects. The discrete-element method (DEM) can represent particle contacts, ice bonds, fabric rearrangement and force chains, but apparatus-scale thermo-hydro-mechanical simulation requires many particles and non-unique micromechanical calibration (Cundall and Strack, 1979; Chang et al., 2023; Krzaczek et al., 2023). The material point method (MPM) is effective for large deformation, thaw collapse, contact and material transport, although grid crossing, multiphase stabilisation and constitutive transfer require care (Sulsky et al., 1994; Bardenhagen and Kober, 2004; J. Yu et al., 2024). Peridynamic and phase-field methods permit fracture or diffuse-interface evolution without explicit crack tracking and are valuable where frost cracking, ice-lens fracture or thaw slumping is the measured mechanism (Silling, 2000; Bourdin et al., 2000; Miehe et al., 2010; Suh and Sun, 2022; Kebria and Na, 2024; Zheng et al., 2024). For the present laboratory data, however, the directly observed quantities are temperature and one-dimensional displacement rather than resolved crack paths; a lower-cost mesoscopic representation is therefore appropriate.

Lattice element methods (LEM) occupy an intermediate scale between particle-resolved DEM and conventional continuum elements. Early framework and rigid-body-spring ideas established that a continuum may be replaced by discrete axial or normal–shear interactions (Hrennikoff, 1941; Kawai, 1978; Ostoja-Starzewski, 2002). Random lattices subsequently captured fracture and transport in cementitious and geomaterials (Schlangen and van Mier, 1992; Bolander and Saito, 1998; Bolander and Sukumar, 2005; Grassl, 2009; Grassl and Bolander, 2016; Nikolic et al., 2016; Rizvi, 2019; Yoshioka et al., 2022). The geometric duality of Delaunay triangulations and Voronoi tessellations is particularly useful: Delaunay edges provide local mechanical connectivity, while dual faces and cells provide control volumes and flux areas (Delaunay, 1934; Voronoi, 1908; Hwang et al., 2022). This separation permits one irregular point cloud to support both sparse bond mechanics and conservative transport. It also exposes bond forces, eigenstrains and local state variables directly, while avoiding the particle count of DEM.

Mechanical behaviour still requires an appropriate constitutive law. Frozen-soil models span temperature-dependent elasticity, Mohr–Coulomb and critical-state plasticity, cap and bounding-surface models, creep, damage, hypoplasticity and thermodynamic hyperplasticity (Xu et al., 2016; Lai et al., 2014; F. Yu et al., 2022; Li et al., 2024; Li and Yin, 2025). Hypoplasticity relates stress rate directly to stress, strain rate and internal state without a conventional yield surface, and intergranular-strain extensions reproduce small-strain stiffness and cyclic reversal (Kolymbas, 1991; von Wolffersdorff, 1996; Niemunis and Herle, 1997; Xu et al., 2016). Hyperplasticity derives recoverable stress and admissible dissipation from free-energy and dissipation potentials, giving a systematic basis for kinematic and isotropic hardening (Collins and Houlsby, 1997; Houlsby and Puzrin, 2000, 2006; Lai et al., 2014). The available freeze–thaw experiments do not uniquely identify a complete multiaxial law; accordingly, the global benchmark simulations use a transparent normal–shear lattice with thermal, ice, segregation and densification eigenstrains, while executable hypoplastic and hyperplastic bond modules are verified separately and documented in the Supplementary Information.

A robust lattice implementation also requires a clear element contract for nonlinear solution and a mechanism for storing irreversible local deformation. The FEAP organization is useful in this respect: every element returns an internal-force residual and a consistent or algorithmic tangent, and the assembled Newton system corrects global nodal unknowns until equilibrium is satisfied (Taylor, 2020; Zienkiewicz et al., 2005). Embedded-discontinuity lattice formulations enrich the regular displacement by a Heaviside jump and retain a local jump residual, allowing concentrated opening, sliding, consolidation or creep to be represented without remeshing (Nikolic et al., 2016; Rizvi, 2019). For frozen soils, the rate term cannot be temperature independent. Creep and constant-strain-rate tests show that frozen-soil deformation accelerates as temperature approaches the melting interval and depends strongly on stress level and phase state (Arenson and Springman, 2005; Xu et al., 2017; Cudmani et al., 2023). These observations motivate the FEAP-compatible edge kernel, jump history and bounded temperature-dependent creep law introduced here.

Scientific-computing architecture is also part of the modelling problem. Sparse direct solvers are robust for small laboratory meshes; preconditioned Krylov methods reduce memory at larger sizes; independent parameter or material cases can be distributed across CPU processes; and GPU sparse solvers may accelerate sufficiently large repeated systems when data remain device resident (Harris et al., 2020; Virtanen et al., 2020; Hunter, 2007; Okuta et al., 2017; Xue et al., 2023). GPU availability alone does not guarantee speedup because matrix assembly, host–device transfer and kernel launch can dominate small problems. Reproducible performance reporting must therefore record the backend actually used, the fallback path, problem size, tolerances and wall time rather than infer acceleration from the presence of GPU commands.

The objective of this study is to develop, verify and experimentally assess an executable axisymmetric Voronoi–Delaunay lattice framework for laboratory freeze–thaw deformation. The contributions are: (i) source-faithful geometries and staged thermal, hydraulic and mechanical boundary conditions for one closed and six open systems; (ii) a dual Delaunay mechanical and Voronoi/circumcentric transport discretization; (iii) a FEAP-compatible edge routine that returns element residual and tangent arrays; (iv) Heaviside jump kinematics in which thaw-consolidation and creep increments are stored as local bond histories; (v) a bounded temperature- and phase-dependent creep law; (vi) sparse CPU-direct, CPU-iterative, process-parallel and optional GPU-conjugate-gradient pathways; (vii) analytical verification and combined mesh–time-step sensitivity analysis; and (viii) one-, two- and revolved three-dimensional post-processing for seven laboratory configurations.

First-cycle displacement endpoints are used for case-level calibration, later KF cycles provide a separate trend check, and all unmeasured internal fields are identified as model predictions. Optional hypoplastic and hyperplastic routines are supplied as separately verified software modules in the Supplementary Information and are not used in the reported global benchmark calculations.

2. Materials and methods

2.1. Laboratory test programme and source datasets

2.1.1. Kieler Förde marine soil: retrieval, storage and material characterization

The KF material was a disturbed deep-marine soil recovered from approximately 30 m depth in Kieler Förde, Baltic Sea, near 54.4685720 N and 10.2695047 E. The available laboratory record states that the material was air dried and retained in an airtight container. Shipboard sealing, transport temperature, storage duration and salinity preservation were not documented and were not inferred. The fraction passing a 1 mm sieve was used and coarser grit was discarded. Under the Unified Soil Classification System, the soil was classified as CL. Reported specific gravity, liquid limit and plasticity index were 2.68, 46.7% and 28.2%, respectively. Maximum dry density was 1.72 g cm^{-3} at an optimum water content of 19.4%.

X-ray fluorescence reported 52.435% SiO_2, 18.294% Al_2O_3, 6.591% Fe_2O_3, 2.838% CaO, 0.384% Na_2O, 1.985% MgO, 3.058% K_2O, 0.977% TiO_2, 0.361% P_2O_5 and 0.037% MnO by mass. The working dry density was 1.1209 g cm^{-3} and the air-dried water content was 2.62%. Specimens were saturated using distilled water. The freeze–thaw specimen water content was 33.46% before testing; a reported post-test value was 47.69%. Because the source description calls the specimen saturated while the mass–volume combination does not independently close to 100% saturation, the database retains both the source statement and the calculated diagnostic instead of silently changing either.

Three laboratory procedures supplied the KF calibration and trend-assessment basis. The pressure-cell flow specimen was 50 mm in diameter and 100 mm high, subjected to 300 kPa cell pressure and an average effective pressure of 225 kPa. The reported steady discharge was 0.21 mL min^{-1} after saturation. It is not converted to hydraulic conductivity because the complete hydraulic gradient and correction details are unavailable. The one-dimensional consolidation specimen was 71.2 mm in diameter and 20 mm high. Stress increased from 12 to 400 kPa and was unloaded to 25 kPa; strain was 0.0549 at 25 kPa during loading and 0.199 at 400 kPa, with 0.3 mm rebound and retained plastic strain 0.12964 after unloading.

2.1.2. KF closed-system freeze–thaw apparatus and protocol

The FT specimen was compacted to 70 mm diameter and 49.7 mm height at the stated dry density. The modified oedometer used a purpose-built ring with peripheral thermocouples near the top, centre and bottom. Helical copper tubing around the outside of the ring circulated brine from a Huber Mini Chiller 300. Two 2 mm solid metallic plates replaced porous stones at the top and bottom, preventing drainage. Vertical displacement and maintained effective stress were recorded using the Wille Geotechnik/GeoSys system, and the complete cell was placed in a climatic chamber. A 25 kPa vertical surcharge was prescribed.

The coolant schedule alternated between approximately −14 °C and 37 °C. Each freezing or thawing branch continued until no obvious additional displacement was observed. The reported branch durations were about 5 h for freezing and 2.5 h for thawing. Eleven cycles were conducted. The source plots distinguish specimen-plus-mould and mould movements; corrected specimen displacement was used. The reported first-cycle heave was 3.78 mm, freezing strain 7.6%, thaw/freezing strain ratio 0.57, initial deformation-rate indicator 1.62 mm h^{-1} and plateau near cycle 7. The implied first-cycle thaw settlement used in the database is $0.57 \times 3.78 = 2.1546$ mm.

2.1.3. Open-system thesis materials and specimen preparation

The independent open-system data were taken from Al-Hussaini's Cardiff University thesis (Al-Hussaini, 2017). Three materials were studied: refined Speswhite kaolin, natural Pegwell Bay soil and cement kiln dust. SK had specific gravity 2.61, liquid limit 68.5%, plastic limit 42.0%, plasticity index 26.5%, shrinkage limit 32.7%, specific surface area 7.63 m^2 g^{-1}, 93.6% clay-size particles and 6.4% silt. X-ray diffraction indicated approximately 95% kaolinite and 4% illite. PB had specific gravity 2.69, liquid limit 29.5%, plastic limit 19.2%, plasticity index 10.3%, shrinkage limit 16%, specific surface area 0.41 m^2 g^{-1}, 7.3% sand, 84.3% silt and 8.4% clay-size material; mineralogy was 78% quartz, 16% calcite and 6% dolomite. CKD had specific gravity 2.72, liquid limit 42%, plastic limit 27%, plasticity index 15%, shrinkage limit 21%, specific surface area 0.58 m^2 g^{-1}, 70% silt and 30% clay-size particles; it contained approximately 85% calcite and 14% silica.

For slurry tests, material was mixed with water to 1.2 times its liquid limit, sealed in plastic bags and airtight containers for at least 48 h, then placed carefully to avoid trapped air. Initial SK, PB and CKD water contents were 82.3, 35.4 and 49.2%; dry unit weights were 8.11, 13.51 and 11.40 kN m^{-3}; and void ratios were 2.148, 0.951 and 1.337. The nominal starting height was 65 mm; heights after consolidation under 2 kPa were 60.40, 59.59 and 62.47 mm.

Compacted specimens were prepared on the wet side of optimum by static compaction at 1.25 mm min^{-1}. SK, PB and CKD were prepared at water contents 30.0, 19.0 and 24.2%; dry unit weights 14.16, 16.91 and 12.50 kN m^{-3}; void ratios 0.808, 0.561 and 1.330; and compaction pressures 740, 652 and 644 kPa. They were saturated for 24 h with the water table at the specimen top. Heights after saturation were 69.79, 65.10 and 65.22 mm. These source-supported heights, rather than a common nominal height, define the numerical geometries.

2.1.4. Open-system apparatus, instrumentation and correction

The thesis apparatus comprised a 103.3 mm internal-diameter PVC specimen mould, an exterior mould, basal acrylic reservoir and porous stone, top cooling/heating chamber, four wall thermocouples, four LVDTs, thermal insulation, Vortex Tube air supply and a System 8000 data-acquisition unit. Specimen thermocouples were initially positioned 4.5, 29.5, 54.5 and 63.5 mm below the top. Type-K probes had a specified range from −50 to 250 °C, 0.7 s response time and class-1 tolerance of 1.5 °C. LVDTs had 50 mm range, 0.2% full-range linearity, 0.3 μm resolution and an operating range from −40 to 120 °C. Temperature and displacement were sampled every minute.

The thermal response of the measuring system was tested with a 100 mm-diameter, 50 mm-high aluminium-alloy dummy specimen. Cooling produced measured chamber/dummy and mould movements of −0.65 and − 0.39 mm; heating produced +0.72 and + 0.33 mm. The thesis calculated and applied the corresponding correction factors. This apparatus correction is important because mould movement approached 1 mm in some soil tests and cannot be neglected when interpreting heave.

For freeze–thaw testing, the top chamber temperature was lowered to approximately −19.5 ± 0.5 °C for 24 h. The basal water level remained at the top of the porous stone, permitting water supply during freezing and drainage during thaw. Thawing occurred at ambient laboratory temperature of approximately 21 ± 2 °C. Nominal surcharge was 2 kPa. Duplicate specimens were used where destructive water-content profiles were required after freezing or thawing. The seven primary numerical cases comprise KF closed, SK/PB/CKD slurry and SK/PB/CKD compacted. Secondary intermittent and wet–freeze–thaw–dry histories are retained for future extension but not used to calibrate the primary cases.

2.1.5. Experimental metrics and uncertainty treatment

Heave was the increase in corrected specimen height from the start of

freezing to the maximum freezing displacement. Thaw settlement was the decrease from that maximum to the end of thaw. Freezing strain used the pre-freezing specimen height; thaw strain used the height at the start of thaw. The numerical equilibrium time is the time to 99% of the branch displacement. The numerical initial-rate indicator is the maximum slope during the first 3 h of freezing. Segregation potential was retained as source data using the thesis definition $SP = v_\phi/\nabla T_f$ with $v_\phi = (\mathrm{d}h/\mathrm{d}t)/1.09$ (Konrad and Morgenstern, 1981; Konrad and Seto, 1994); it was not used as a calibration or validation target because the present code does not resolve a discrete active ice lens.

Uncertainty is constrained by the available record. The KF source does not provide replicate statistics or complete raw synchronized files. The thesis provides instrument specifications, duplicate destructive specimens and apparatus corrections, but not confidence intervals on all final values. Accordingly, the comparison uses absolute and percentage errors without inferential statistics. Source inconsistencies are retained transparently: the PB diameter appears as both 103.3 and 103.5 mm; the apparatus drawing value 103.3 mm is used. The slurry PB segregation potential appears as 2.88 in the traceable table and 3.10 in narrative text; 2.88 is retained.

2.1.6. Experimental benchmark matrix and plotted response

Tables 2–4 form the traceable input matrix for numerical calibration and evaluation. Material properties are separated from specimen-state variables, and both are separated from response targets. Fig. 4 plots the measured endpoints before numerical results are introduced. This arrangement prevents the simulation from obscuring the experimental evidence and makes explicit which observations are directly measured, which are calculated from measured geometry and which are unavailable. No synthetic continuous laboratory history is introduced where only stage endpoints were supplied. (See Fig. 1.)

2.1.7. Evidence hierarchy and terminology

The terminology is fixed throughout the manuscript. *Verification* denotes comparison with analytical or independently controlled numerical solutions and includes the radial-conduction, Stefan-front, confined-compression, resolution and backend-consistency tests. *Calibration* denotes adjustment of unmeasured model coefficients to reproduce the first-cycle heave and thaw-settlement endpoints. The six open-system calculations are therefore described as calibrated benchmark reproductions rather than independent validations. *Validation* is reserved for information not used in endpoint calibration; in the present data this is limited to the qualitative reduction and plateau of the KF response over cycles 2–11. The non-reoptimised FEAP jump–creep calculations are termed cross-formulation benchmark checks. Temperature, ice fraction, total-water redistribution, cryogenic pressure proxy, bond stress and freezing-front location are model predictions unless a source measurement is explicitly plotted against them.

2.2. Numerical model development

2.2.1. Software organization and reproducible implementation

The executable reference code was written in Python and uses NumPy for array state, SciPy for Delaunay triangulation and sparse linear algebra, pandas for tables, Matplotlib for two- and three-dimensional graphics, Shapely for clipped Voronoi visualisation and optional CuPy/cupyx for GPU sparse CG (Harris et al., 2020; Virtanen et al., 2020; Hunter, 2007; Okuta et al., 2017). Input data are stored in immutable material and experimental-target records. Configuration objects store geometry, mesh controls, thermal/hydraulic/mechanical coefficients, schedule and solver options. Results contain the mesh, complete histories, selected full-field snapshots, solver metadata and derived metrics. A fixed random seed makes irregular meshes reproducible.

The repository contains separate modules for material data, mesh/solver physics, case execution, analytical benchmarks, process-parallel timing, optional nonlinear constitutive laws and figure generation. Running the top-level workflow regenerates all seven cases, tables, 1D

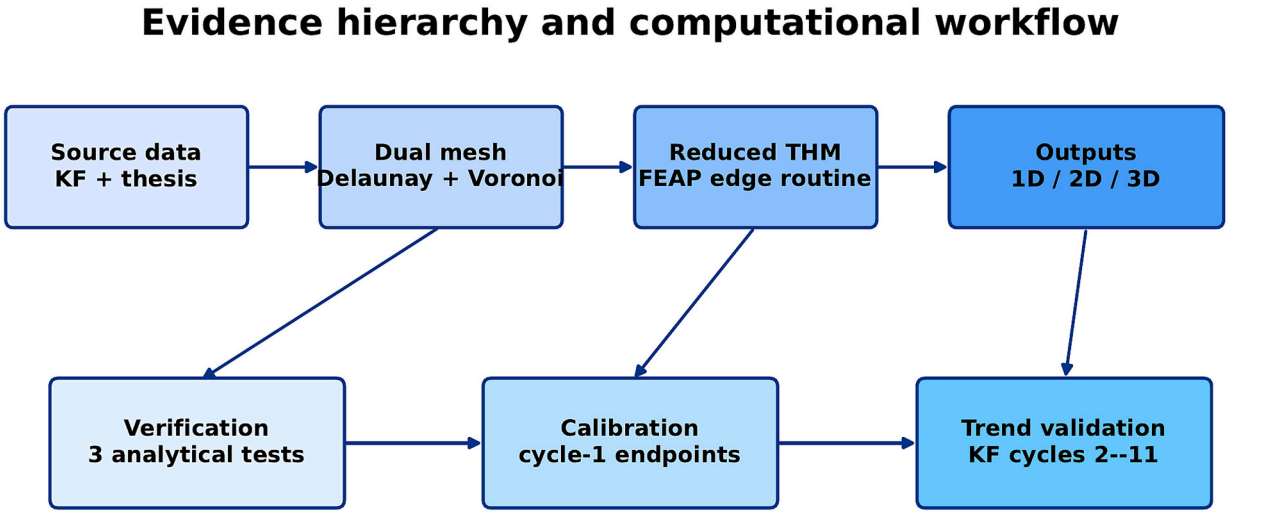

Fig. 1. Architecture and evidence hierarchy of the executable lattice framework. Measured source data, modelling priors, pre-processing, coupled solution, post-processing, verification, endpoint calibration, trend assessment and prediction/transfer operations are stored as distinct objects.

comparisons, 2D fields, revolved 3D views and the verification figures. The code records whether a linear system was solved by CPU direct, CPU iterative or GPU CG and records the cause of any fallback.

2.2.1.1. AI-assisted software development. OpenAI ChatGPT was used as a development aid for code structuring, debugging, documentation and manuscript organization. The experimental inputs were taken from the cited source records. The authors reviewed the governing equations, parameter mappings, references, source code and generated outputs, executed the reproducible reference workflow, and retain full responsibility for the scientific content and software.

2.2.2. Problem geometry, initial fields and staged loading

Each apparatus was represented by a meridional axisymmetric domain

$$\Omega = \{(r,z) : 0 \le r \le R\,, 0 \le z \le H\}. \tag{1}$$

For KF, $R = 35.0\,\text{mm}$ and $H = 49.7\,\text{mm}$. For the six open-system cases, $R = 51.65\,\text{mm}$ and H was set to the measured height immediately before freezing: 60.40, 59.59 and 62.47 mm for the SK, PB and CKD slurries, and 69.79, 65.10 and 65.22 mm for the compacted states. The initial temperature was spatially uniform at the reported laboratory temperature, the initial total-water content was obtained from the source water content, dry density, specific gravity and reported saturation state, the initial ice fraction was zero, and the creep, consolidation, damage and cyclic-history variables were set to zero. A mechanical preload solve under the prescribed surcharge established the reference displacement before thermal cycling.

The mechanical boundary conditions were common to all cases: $u_r = 0$ on the axis, $u_r = 0$ at the rigid ring, $u_z = 0$ at the base, and a uniform vertical traction of 25 kPa for KF or 2 kPa for the open columns on the top surface. For KF, outer-wall Robin exchange imposed the $-14/37$°C cooling–heating programme, the top and bottom thermal fluxes were zero, and every hydraulic boundary was no-flow. For the open columns, the top exchanged heat with the -19.5 ± 0.5°C freezing chamber for 24 h, the base remained warm and hydraulically connected to a reservoir, the cylindrical wall was insulated, and thawing occurred toward ambient temperature. The model schedule was divided into six reporting stages: initial/preload, early freezing, mid freezing, end freezing, mid thawing and end thawing. KF continued through 11 cycles for the cyclic calculation; the other six configurations used one freeze–thaw cycle, consistent with the primary source tests.

2.2.3. Delaunay lattice and circumcentric/Voronoi dual

The axisymmetric domain $\Omega \subset (r,z)$ is populated by a perturbed tensor-product point cloud supplemented by exact nodes on the axis, wall, top and bottom. A seeded perturbation removes directional bias while preserving the rectangular specimen boundary. The Delaunay triangulation $\mathscr{T}$ is constructed from points $\mathbf{x}_i = (r_i, z_i)$. Every unique Delaunay edge e_{ij} has length

$$L_{ij} = \|\mathbf{x}_j - \mathbf{x}_i\|, \qquad \mathbf{n}_{ij} = \frac{\mathbf{x}_j - \mathbf{x}_i}{L_{ij}}, \qquad \mathbf{t}_{ij} = (-n_z, n_r). \tag{2}$$

The dual-face length l_{ij}^* is the distance between circumcentres of adjacent triangles; a positive lower bound is used on boundary or obtuse configurations. The two-dimensional nodal storage area A_i^* is the sum of one-third of each incident triangle area. Axisymmetric nodal volume and dual-face area are

$$V_i = 2\pi r_i^{\text{eff}} A_i^*, \qquad A_{ij}^* = 2\pi r_{ij}^{\text{eff}} l_{ij}^*, \tag{3}$$

where r^{eff} regularizes the symmetry axis using half a reference radial spacing. A scalar transport coefficient χ gives the edge conductance

$$G_{ij}^{\chi} = \chi_{ij} \frac{A_{ij}^*}{L_{ij}}. \tag{4}$$

Assembly of $+G$ on edge-end diagonals and $-G$ off diagonal gives a symmetric graph Laplacian. Full geometric derivations, boundary surface measures and quality metrics are given in Supplementary Information, Appendix A.

The preprocessing sequence is deterministic. A nominal $n_r \times n_z$ tensor-product cloud is generated, only interior points are perturbed by a seeded fraction of the local spacing, exact axis/wall/top/bottom points are reinserted, and triangles outside the rectangular meridional domain or below the area tolerance are rejected. Unique edges, edge directions, incident triangles, circumcentres, positive dual-face lengths, nodal areas and boundary sets are then generated once and stored. The principal FEAP jump–creep calculations used 143 nodes, 218 triangles and 360 Delaunay edges. Mean minimum triangle angles were 29.8–33.2° among the seven geometries; isolated near-boundary slivers were handled by the positive dual-length lower bound and were included in the mesh-sensitivity check rather than silently deleted. The initial topology remains fixed during freezing and thawing; changing the specimen geometry or mesh density triggers complete preprocessing.

2.2.4. Thermal field and smooth phase partition

The reduced energy equation is

$$C_{\text{app}}(T,\theta_w)\dot{T} = \nabla\cdot(k(T,S_{\text{i}})\nabla T), \tag{5}$$

with a smooth ice fraction

$$S_{\text{i}}(T) = \left[1 + \exp\left(\frac{T - T_f}{\Delta T_f}\right)\right]^{-1}. \tag{6}$$

Total volumetric water θ_w is partitioned as $\theta_i = S_{\text{i}}\theta_w$ and $\theta_l = (1 - S_{\text{i}})\theta_w$. The apparent volumetric heat capacity is

$$C_{\text{app}} = \rho C + L_v S_{\text{i}}(1 - S_{\text{i}})/\Delta T_f, \tag{7}$$

where L_v is an effective volumetric latent-heat parameter. Conductivity is interpolated between warm and frozen values. Backward Euler time integration gives

$$\left(\frac{\mathbf{M}_T}{\Delta t} + \mathbf{K}_T\right)\mathbf{T}^{n+1} = \frac{\mathbf{M}_T}{\Delta t}\mathbf{T}^n + \mathbf{q}_\Gamma, \tag{8}$$

where $M_{T,ii} = V_i C_{\text{app},i}$. Robin thermal exchange adds $hA_{\Gamma,i}$ to the diagonal and $hA_{\Gamma,i}T_\infty$ to the right-hand side. KF applies this exchange to the outer wall; open cases apply it to the top and bottom.

2.2.5. Reduced total-water redistribution and cryogenic potential

A reduced total-water equation was used because the source data do not provide complete retention, unfrozen-water and hydraulic functions for every material:

$$\dot{\theta}_w = \nabla\cdot\left[D(S_{\text{i}})\nabla\left(\theta_w - \theta_{\text{eq}}\right)\right], \tag{9}$$

where $D(S_{\text{i}}) = D_f + \left(D_u - D_f\right)(1 - S_{\text{i}})^m$. A Clapeyron-type cryogenic pressure is

$$p_{\text{cryo}} = \frac{\rho_w L_f}{T_0}\langle T_f - T\rangle_+, \tag{10}$$

and the local equilibrium tendency is $\theta_{\text{eq}} = \text{clip}\left(\theta_0 + C_c p_{\text{cryo}}, \theta_{\min}, \theta_{\max}\right)$. The implicit discrete equation uses the same dual conductance operator as heat. Closed boundaries have zero flux; the open basal boundary prescribes $\theta_w = \theta_{\text{reservoir}}$ by a large penalty. A reduced pressure/storage diagnostic is $p^* = K_\theta(\theta_w - \theta_0)$. It drives

densification but is not reported as measured pore pressure.

Eqs. (9)–(10) are a reduced-order redistribution model. They do not solve Darcy or Richards flow in hydraulic-head form, do not enforce a Biot effective-stress balance, and do not nucleate or grow discrete ice lenses. The imposed open basal value permits numerical exchange of the bounded total-water variable, whereas the closed case prohibits that exchange. Consequently, the calculated water, cryogenic-pressure and phase-front fields are predictions conditioned on the selected coefficients and boundary values; they are not direct reconstructions of measured pore pressures or water-content profiles. The displacement calibration alone cannot identify a unique internal water-migration mechanism.

2.2.6. Lattice kinematics, eigenstrains and displacement jumps

For edge $e = (i,j)$, the four nodal degrees of freedom are $\mathbf{d}_e = \left[u_{r,i}, u_{z,i}, u_{r,j}, u_{z,j}\right]^{\top}$. Normal and shear operators are

$$\mathbf{B}_n = \frac{1}{L_e}[-n_r, -n_z, n_r, n_z], \qquad \mathbf{B}_s = \frac{1}{L_e}[-t_r, -t_z, t_r, t_z], \tag{11}$$

so that the regular strains are $\varepsilon_n = \mathbf{B}_n\mathbf{d}_e$ and $\gamma_s = \mathbf{B}_s\mathbf{d}_e$. The displacement difference is also the edge jump, $[[\mathbf{u}]]_e = \mathbf{u}_j - \mathbf{u}_i$. To represent localized time-dependent deformation without remeshing, the edge displacement is enriched by a regularized Heaviside function,

$$\mathbf{u}(x) = \overline{\mathbf{u}}(x) + H_{\Gamma_e}(x)\boldsymbol{\alpha}_e, \qquad \boldsymbol{\alpha}_e = \alpha_n\mathbf{n}_e + \alpha_s\mathbf{t}_e, \tag{12}$$

where Γ_e is the local discontinuity section and $\boldsymbol{\alpha}_e$ is a history jump. In the corresponding one-dimensional edge coordinate the generalized gradient is

$$\mathcal{G}_{\Gamma_e}(x) = -\frac{1}{L_e} + \delta_{\Gamma_e}(x), \tag{13}$$

which satisfies zero mean over the edge and recovers the strong-discontinuity form used in embedded lattice elements (Nikolic et al., 2016; Rizvi, 2019). The executable production route updates $\boldsymbol{\alpha}_e$ locally and therefore introduces no additional global degree of freedom; the full local residual required for static condensation is included in the Supplementary Information and FEAP template.

The normal eigenstrain excluding localized history is

$$\varepsilon_e^0 = \alpha_T(\overline{T}_e - T_0) + \beta_i\overline{\theta}_{i,e} + \beta_s\langle\overline{\theta}_{w,e} - \theta_0\rangle_+\overline{S}_{i,e} + w_{z,e}\xi_e, \tag{14}$$

where $w_{z,e} = |n_z|^b$. Persistent thaw consolidation is represented by a signed normal jump $\alpha_n^c = -L_e w_{z,e}\zeta_e$. Creep contributes $\alpha_n^{cr} = L_e\varepsilon_n^{cr}$ and $\alpha_s^{cr} = L_e\gamma_s^{cr}$. The mechanical strains passed to the bond law are consequently

$$\varepsilon_n^m = \mathbf{B}_n\mathbf{d}_e - \varepsilon_e^0 - \frac{\alpha_n^c + \alpha_n^{cr}}{L_e}, \qquad \gamma_s^m = \mathbf{B}_s\mathbf{d}_e - \frac{\alpha_s^{cr}}{L_e}. \tag{15}$$

Warm and frozen moduli are interpolated with ice fraction, $E = E_u + (E_f - E_u)S_i$ and $G = E/[2(1+\nu)]$. The Delaunay edge area is the corresponding axisymmetric dual-face area. An elastic hoop term $E_i V_i / r_i^2$ stabilizes the circumferential strain and enforces axisymmetric consistency.

2.2.7. Fixed-reference kinematics and range of applicability

The global lattice calculation uses a fixed Delaunay topology and infinitesimal edge strain. Nodal coordinates, dual volumes and transport-face areas are not updated during the cycle. The reported 26–35% axial strains in several open-system tests therefore exceed the range in which the internal stress and strain fields can be interpreted as a rigorous small-strain continuum solution. For those cases the model is used as a reduced-order mapping from imposed thermal/hydraulic conditions to specimen-top displacement on the original geometry. The calibrated displacement endpoints remain useful for apparatus-scale screening, but local stress, water and deformation contours should be interpreted qualitatively. The revolved graphics likewise display predicted fields on the reference cylinder. Finite-strain transfer would require an updated-Lagrangian or material-point formulation with volume, porosity, face-area and constitutive updates.

2.2.8. Temperature-dependent creep and thaw-consolidation update

Frozen-soil creep was represented by a bounded Norton–Glen relation motivated by the observed stress- and temperature-dependent behaviour of frozen soils near the melting interval (Arenson and Springman, 2005; Xu et al., 2017; Cudmani et al., 2023):

$$\dot{\varepsilon}_n^{cr} = A_{\mathrm{ref}}a_T(T,S_i)\left(\frac{|\sigma_n'|}{\sigma_{\mathrm{ref}}}\right)^{n_c}\mathrm{sgn}(\sigma_n'), \tag{16}$$

with an analogous shear expression. The temperature–phase shift is

$$a_T = \mathrm{clip}\Big[\exp\left\{-\frac{Q}{R_g}\left(\frac{1}{T_K} - \frac{1}{T_{K,\mathrm{ref}}}\right)\right\} \times\left(S_i^{m_c} + 4c_tS_i(1-S_i) + c_u(1-S_i)\right), a_{\min}, a_{\max}\Big]. \tag{17}$$

The Arrhenius term increases the rate as temperature approaches the reference melting interval, while the phase-window term prevents unrealistically large extrapolation in fully unfrozen material. A semi-implicit local update evaluates the elastic predictor, advances the creep strain, and supplies the positive algorithmic modulus

$$E_{\mathrm{alg}} = \frac{E}{1 + E\Delta t\,\partial\dot{\varepsilon}^{cr}/\partial\sigma'}, \qquad 0.25E \le E_{\mathrm{alg}} \le E. \tag{18}$$

The creep strain and jump are bounded because the available tests are short-duration freeze–thaw tests rather than dedicated creep experiments. The parameters are therefore literature-informed priors, not measured material constants.

The thaw-consolidation variable follows the existing bounded evolution law, but its mechanical action is now explicit through α_n^c. It grows during melting in proportion to the pressure/storage drive and remaining capacity, and is inactive during freezing. This separation distinguishes reversible phase expansion, persistent consolidation and rate-dependent creep in the output fields. It also allows the model to show that short-term creep is secondary to consolidation for the present tests rather than hiding both mechanisms in a single fitted eigenstrain.

2.2.9. FEAP-compatible element residual and tangent

Following the FEAP convention, every edge routine returns an element residual $\mathbf{P}_e$ and tangent $\mathbf{S}_e$ (Taylor, 2020). With total normal stress $\sigma_n = \sigma_n' - \alpha_B p^*$ and shear stress τ_s, the edge contribution is

$$\begin{aligned}\mathbf{P}_e &= A_eL_e\left(\mathbf{B}_n^{\top}\sigma_n + \mathbf{B}_s^{\top}\tau_s\right) - \mathbf{f}_e^{\mathrm{ext}},\\ \mathbf{S}_e &= A_eL_e\left(E_{\mathrm{alg}}\mathbf{B}_n^{\top}\mathbf{B}_n + G_{\mathrm{alg}}\mathbf{B}_s^{\top}\mathbf{B}_s\right).\end{aligned} \tag{19}$$

The global residual and tangent are $\mathbf{P} = \sum_e \mathscr{A}_e\mathbf{P}_e$ and $\mathbf{S} = \sum_e \mathscr{A}_e\mathbf{S}_e + \mathbf{S}_\theta$, where $\mathbf{S}_\theta$ is the hoop contribution and $\mathscr{A}_e$ is the Boolean assembly operator. Essential constraints are imposed after assembly, and Newton correction solves

$$\mathbf{S}^{(k)}\Delta\mathbf{d}^{(k)} = -\mathbf{P}^{(k)}, \qquad \mathbf{d}^{(k+1)} = \mathbf{d}^{(k)} + \Delta\mathbf{d}^{(k)}. \tag{20}$$

The executable Python edge kernel stores temperature, phase, creep strain, consolidation jump, stress and dissipation as bond history arrays. A companion Fortran user-element template maps nodal coordinates and degrees of freedom to FEAP arrays xl and ul, returns s and p, and reserves hr for history. The template documents portability but was not compiled inside the FEAP program in the present environment.

2.2.10. Separately verified hypoplastic and hyperplastic software modules

The software package also contains frozen-soil hypoplastic and hyperplastic bond routines. These modules were exercised only in independent material-point tests of monotonic compression and cyclic shear. They were not activated in any of the seven global freeze–thaw benchmark calculations because the available laboratory records do not provide the multiaxial stress paths, shear strains, tensile response or cyclic strength data required for calibration. They therefore make no contribution to the reported global endpoint errors, field plots or CPU timing. Their governing equations, state variables, local integration algorithms and separate verification results are provided in Supplementary Information, Appendix D, as extensibility modules for future datasets.

2.2.11. Staggered time integration and global solution

The coupled problem is solved sequentially at each time step. Thermal coefficients are evaluated from the current phase state, the implicit thermal system is solved, phase and apparent heat capacity are updated, the implicit total-water system is solved, cyclic and consolidation states are updated, the local temperature-dependent creep problem is integrated on every edge, and the FEAP residual–tangent system is assembled and solved. Under-relaxation is available for thermal and water fields. Because the mechanical solve is quasi-static, no inertial time integration is introduced. The full Newton edge kernel and the faster production route use the same residual/tangent interface; the production route updates local jumps once per staggered step and then performs one sparse equilibrium solve, which was stable for the laboratory cases.

Listing 1. Pseudocode 1: pre-processing and staggered coupled solution.

```
INPUT source material record, case geometry, boundary schedule, model
    priors
seed random generator
create interior point cloud and exact axis/wall/top/bottom nodes
Delaunay triangulate points
extract unique edges, lengths, directions and attached triangles
compute triangle areas, circumcentres, dual lengths, nodal areas
rotate dual measures to axisymmetric nodal volumes and edge-face areas
identify boundary sets and calculate mesh-quality diagnostics
initialize T, total water, phase fractions, cyclic states and
    displacement
solve initial mechanical equilibrium; store reference displacement
for step = 1 ... Nstep
    determine cycle, freezing/thawing branch and boundary values
    assemble and solve implicit thermal system
    update ice fraction, liquid/ice water and apparent heat capacity
    assemble and solve implicit total-water redistribution system
    impose basal reservoir only for open-system cases
    update cryogenic pressure, freezing dilation and thaw densification
    for each Delaunay edge
        compute Heaviside jump operators and generalized strain
        update temperature-dependent normal and shear creep
        form consolidation and creep jump histories
        return FEAP element residual P_e and tangent S_e
    end for
    assemble global residual/tangent, hoop resistance and surcharge
    solve S Delta d = -P; update quasi-static mechanical equilibrium
    calculate histories, bond jumps, stresses and benchmark metrics
    store requested full-field snapshot
end for
export CSV/JSON/NPZ/VTK and generate 1D, 2D and revolved 3D plots
```

2.2.12. CPU, process-parallel and GPU-hybrid implementation

The CPU-direct mode uses sparse LU through SciPy's sparse direct interface. The iterative mode uses diagonally preconditioned conjugate gradients with relative tolerance 10^{-9} and a maximum iteration count; non-convergence triggers direct solution. Independent cases are parallelized with a process pool. Each process owns its mesh and state, eliminating synchronization within a time step and making the strategy suitable for material sweeps, calibration and uncertainty analysis.

The optional GPU mode uses CuPy and cupyx sparse CSR/CG. Sparse triplet assembly remains on the CPU in the reference code. The matrix and right-hand side are transferred, the GPU solution is attempted, and the vector is gathered. Import failure, allocation failure or nonzero CG status triggers CPU CG and then direct solution. All backend choices and fallback messages are stored in the result. A measured device speedup requires a named GPU, repeated timings after warm-up, consistent precision, transfer-time reporting and meshes large enough to exceed overhead.

Listing 2. Pseudocode 2: backend selection, CPU parallelism and GPU fallback.

```
function LINEAR_SOLVE(A, b, requested_backend)
    convert A to CSR
    if requested_backend == GPU_CG
        try
            transfer A and b to GPU
            solve with cupyx preconditioned conjugate gradient
            if converged: gather x; record GPU_CG; return x
        catch exception
            record GPU failure and continue
        end try
        requested_backend = CPU_ITERATIVE
    end if
    if requested_backend == CPU_ITERATIVE
        build diagonal preconditioner
        solve with SciPy conjugate gradient
        if converged: record CPU_ITERATIVE; return x
        record iterative failure
    end if
    solve with sparse direct factorization
    record CPU_DIRECT; return x
end function

parallel for case in independent_cases using process pool
    build case mesh and run complete staggered transient solution
    write isolated result object
end parallel
```

2.2.13. Consolidation and mechanical-parameter extraction

The supplied data support one-dimensional consolidation parameters but not a unique frozen-soil strength envelope. For any stress interval, the apparent constrained modulus and coefficient of volume compressibility are

$$M_{1D} = \frac{\Delta\sigma_v}{\Delta\varepsilon_v}, \qquad m_v = M_{1D}^{-1}. \tag{21}$$

For the KF test, secant values were calculated for 0–25 and 25–400 kPa; the apparent unloading modulus used the 0.3 mm rebound over the 20 mm specimen height and the 375 kPa stress reduction. For the three slurry materials, C_v, m_v and $k = C_v m_v \gamma_w$ were taken directly from the thesis consolidation table. An indicative competition between consolidation and thaw duration was defined as

$$\Pi_c = \frac{H^2}{C_v t_T}, \tag{22}$$

where H is the specimen height and t_T the scheduled thaw duration. $\Pi_c > 1$ indicates that the diffusion/consolidation time is longer than the imposed thaw stage. This is a screening ratio, not a replacement for the full Morgenstern–Nixon thaw-consolidation ratio.

No unconfined compression, direct shear, triaxial, tensile or frozen creep-strength tests were supplied for the seven states. Consequently, cohesion, friction angle, tensile strength and creep rupture strength cannot be calculated from the available data. The strength values in the optional bond-law files are explicitly labelled modelling priors and are excluded from validation claims. The calculated quantities reported in the Results are constrained moduli, compressibility, hydraulic

Table 1
Numerical controls used for the reported global benchmark calculations. The resolution sequence changes mesh density and time step together and is therefore a combined discretization study, not an isolated spatial-convergence test.

Control	Selected value	Implementation role
Nominal point grid	$n_r \times n_z = 8 \times 12$	Interior point-cloud basis before exact boundary nodes are reinserted.
Realized mesh	143 nodes, 218 triangles, 360 edges	Same topology used by transport and mechanical operators.
Interior jitter	0.12 of local grid spacing	Seeded perturbation used to reduce directional bias.
Random seed	42	Reproduces all reported meshes.
Global minimum angle	0.42–0.51°	Isolated boundary slivers; mean minimum angle is 29.8–33.2°.
Dual-face regularization	$l^*_{ij} \geq 0.25\ L_{ij}$	Prevents negative or vanishing conductances near boundaries and obtuse pairs.
Axis regularization	$r_eff \geq 0.5\ \Delta r$	Prevents zero axisymmetric storage and face areas at $r = 0$.
Boundary-coordinate tolerance	10^{-9} m	Identifies axis, wall, top and bottom nodes.
Time step	300 s (KF); 600 s (open cases)	Backward-Euler thermal and reduced-water updates.
Linear tolerance	10^{-9}	Relative tolerance for CPU/GPU iterative solves.
FEAP local/global tolerances	10^{-10} / 10^{-6}	Local jump update and global residual criteria in the enrichment checks.
Field relaxation	0.75	Optional staggered thermal/water under-relaxation.
Resolution sequence	(5 × 7, 600 s); (6 × 9, 600 s); (8 × 12, 300 s); (10 × 15, 180 s)	Combined refinement sequence used in Fig. 6.

Table 2
Source-derived material properties used to define the laboratory and numerical benchmark matrix. "n.r." denotes not reported as a numerical value in the supplied source. KF oxide values are XRF compositions; SK, PB and CKD composition values are XRD mineral estimates.

Property	Kieler Förde (KF)	Speswhite kaolin (SK)	Pegwell Bay soil (PB)	Cement kiln dust (CKD)
Material description	Baltic marine clay	Refined kaolinite-rich clay	Natural aeolian/periglacial soil	Cement-manufacturing dust
USCS classification	CL	CH	CL	ML
Specific gravity, G_s	2.68	2.61	2.69	2.72
Liquid limit (%)	46.7	68.5	29.5	42.0
Plastic limit (%)	18.5[a]	42.0	19.2	27.0
Plasticity index (%)	28.2	26.5	10.3	15.0
Sand/silt/clay (%)	n.r.[b]	0/6.4/93.6	7.3/84.3/8.4	0/70/30
Specific surface area ($m^2\ g^{-1}$)	n.r.	7.63	0.41	0.58
Optimum water content (%)	19.4	26.7	16.2	27.6
Maximum dry density or unit weight	1.72 Mg m^{-3}	14.56 kN m^{-3}	17.27 kN m^{-3}	14.86 kN m^{-3}
Dominant composition	SiO_2 52.435%; Al_2O_3 18.294%	Kaolinite 95%; illite 4%	Quartz 78%; calcite 16%; dolomite 6%	Calcite 85%; silica 14%

[a] Calculated from PL = LL − PI because the supplied KF source reports LL and PI.
[b] The KF grain-size distribution is provided graphically in the source but not as a complete numerical sand/silt/clay table.

Table 3
Experimental specimen states, boundary conditions and thermal schedules. Heights are the pre-freezing heights after consolidation or saturation for the open-system cases.

Case	Initial state	Geometry, load and cycles	Water content, density and void ratio	Thermal and hydraulic schedule
KF closed	Compacted marine clay saturated with distilled water	70.0 × 49.7 mm; 25 kPa; 11 cycles	w = 33.46%; ρd = 1.1209 Mg m^{-3}; e not reported	Outer-wall forcing at −14/37 °C; closed top and bottom; 5 h freezing and 2.5 h thawing
SK slurry	Saturated slurry at 1.2 LL	103.3 × 60.40 mm; 2 kPa; one cycle	w = 82.3%; γd = 8.11 kN m^{-3}; e = 2.148	Top at −19.5 ± 0.5 °C for 24 h; ambient thaw; open basal reservoir
PB slurry	Saturated slurry at 1.2 LL	103.3 × 59.59 mm; 2 kPa; one cycle	w = 35.4%; γd = 13.51 kN m^{-3}; e = 0.951	Top at −19.5 ± 0.5 °C for 24 h; ambient thaw; open basal reservoir
CKD slurry	Saturated slurry at 1.2 LL	103.3 × 62.47 mm; 2 kPa; one cycle	w = 49.2%; γd = 11.40 kN m^{-3}; e = 1.337	Top at −19.5 ± 0.5 °C for 24 h; ambient thaw; open basal reservoir
SK compacted	Wet-side static compaction and 24 h saturation	103.3 × 69.79 mm; 2 kPa; one cycle	w = 30.0%; γd = 14.16 kN m^{-3}; e = 0.808	Top at −19.5 ± 0.5 °C for 24 h; ambient thaw; open basal reservoir
PB compacted	Wet-side static compaction and 24 h saturation	103.3 × 65.10 mm; 2 kPa; one cycle	w = 19.0%; γd = 16.91 kN m^{-3}; e = 0.561	Top at −19.5 ± 0.5 °C for 24 h; ambient thaw; open basal reservoir
CKD compacted	Wet-side static compaction and 24 h saturation	103.3 × 65.22 mm; 2 kPa; one cycle	w = 24.2%; γd = 12.50 kN m^{-3}; e = 1.330	Top at −19.5 ± 0.5 °C for 24 h; ambient thaw; open basal reservoir

Table 4
Measured freeze–thaw response values used as model-evaluation targets. Panel (a) reports the deformation endpoints and strains; panel (b) reports the rate and segregation descriptors. The KF thaw strain is derived from the reported thaw settlement and frozen height. The KF rate is an initial deformation-rate indicator, whereas the open-system rates are steady-stage heave rates used in the thesis segregation-potential calculations.

(a) Stage-end deformation and strain

Case	Heave (mm)	Freezing strain (%)	Thaw settlement (mm)	Thaw strain (%)	Heave minus settlement (mm)
KF closed	3.780	7.60	2.155	4.03	1.625
SK slurry	21.100	35.0	25.600	31.4	−4.500
PB slurry	16.300	27.3	14.200	18.7	2.100
CKD slurry	16.400	26.2	19.400	24.6	−3.000
SK compacted	20.900	30.0	6.200	6.8	14.700
PB compacted	21.700	33.3	17.700	20.4	4.000
CKD compacted	22.900	35.1	19.900	22.6	3.000

(b) Rate and segregation descriptors

Case	Heave-rate metric (mm h^{-1})	SP ($mm^2°C^{-1}\ h^{-1}$)
KF closed	1.62	–
SK slurry	1.12	2.85
PB slurry	0.85	2.88
CKD slurry	0.71	2.25
SK compacted	0.77	3.74
PB compacted	1.06	4.22
CKD compacted	1.01	4.04

conductivity, relative compaction and mobilized model stresses, not measured strength parameters.

2.2.14. Calibration, verification, validation and error metrics

Measured parameters and model parameters were separated. Geometry, water content, density, index properties, surcharge, schedule and drainage were fixed from source data. Unreported thermal, phase and mechanical coefficients were initialized from literature ranges and calibrated in stages against first-cycle displacement endpoints: thermal timing and profile class first, peak heave through phase/segregation

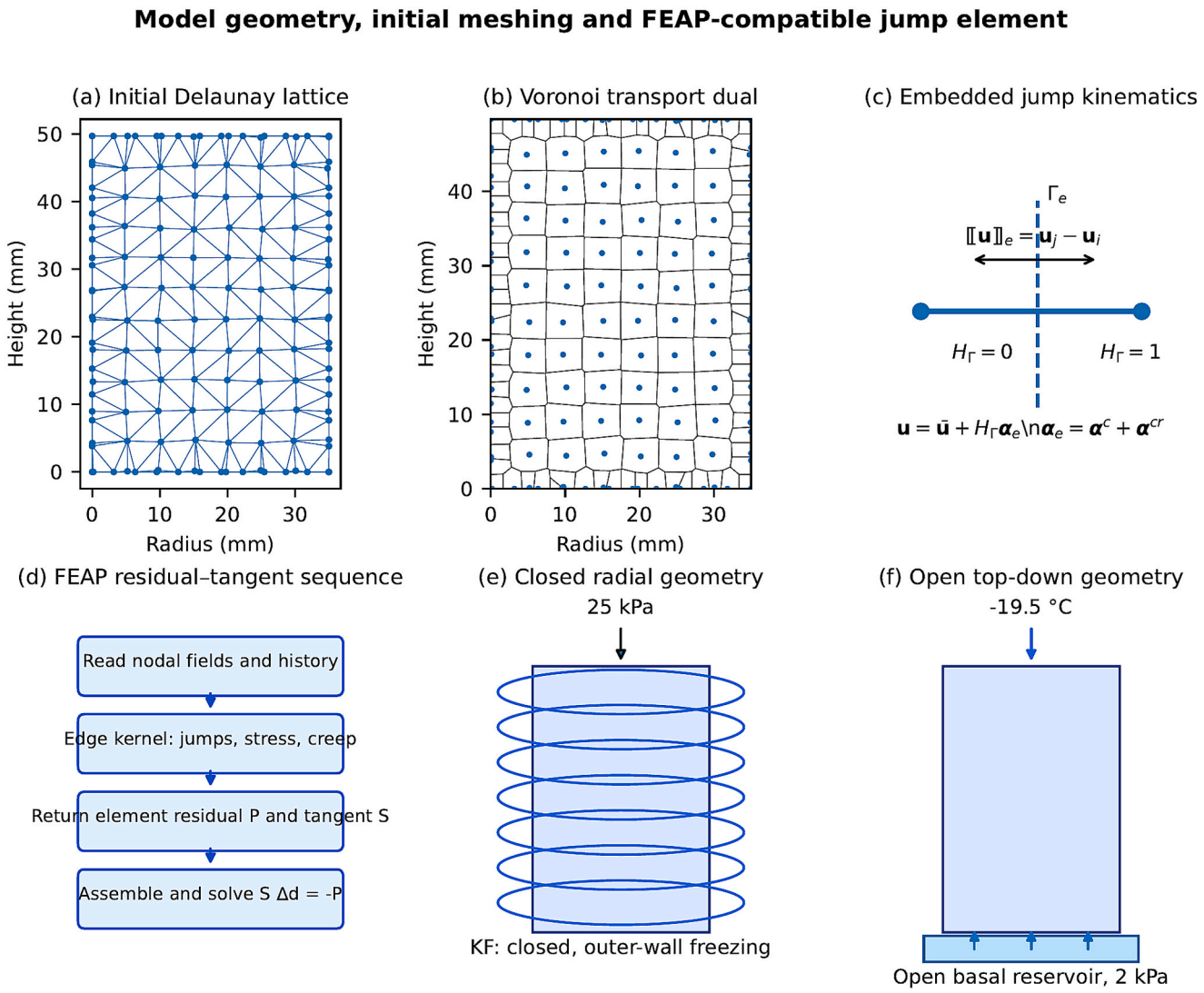

Fig. 2. Detailed numerical setup. (a) Initial Delaunay mechanical lattice; (b) Voronoi/circumcentric transport dual; (c) embedded displacement-jump kinematics; (d) FEAP-compatible element residual–tangent sequence; (e) closed KF outer-wall geometry; and (f) open top-down geometry with basal reservoir. The same point cloud is used for transport and mechanics, but the primal and dual measures have distinct roles.

coefficients, and thaw settlement through densification/recovery. No continuous laboratory curve was fabricated.

Numerical verification comprises the analytical heat, Stefan-front and confined-compression tests, the combined resolution study and backend consistency. The resolution sequence listed in Table 1 changes mesh density and time step simultaneously; it demonstrates convergence of the combined discretization but does not isolate spatial and temporal orders. The six open-system endpoint comparisons are calibrated benchmark reproductions. Independent validation is limited to the reported KF cycle-to-cycle reduction and plateau after the first calibrated cycle. The FEAP jump–creep rerun is a non-reoptimised cross-formulation check.

Analytical verification used relative L_2 error, maximum absolute error and confined-compression displacement error. Experimental endpoint comparison used

$$\mathrm{APE} = 100\left|\frac{y_{\mathrm{sim}} - y_{\mathrm{exp}}}{y_{\mathrm{exp}}}\right|, \qquad \mathrm{MAE} = \frac{1}{N}\sum_{i=1}^{N}\left|y_{\mathrm{sim},i} - y_{\mathrm{exp},i}\right|. \tag{23}$$

Full-curve RMSE and R^2 were not calculated because original synchronized digital records were not available for every case. Water-content profiles, pore pressures and freezing-front positions were not used as quantitative validation metrics. Mesh/backend tests used identical material parameters and fixed random seeds. The four-worker benchmark used the same seven coarse cases in serial and process-parallel execution; speedup was $S_p = t_{\mathrm{serial}}/t_{\mathrm{parallel}}$.

2.2.15. *Post-processing and three-dimensional visualisation*

At selected steps the code stores nodal T, S_i, θ_w, θ_i, θ_l, p_{cryo}, p^*, ξ, ζ, u_r and u_z, together with bond normal/shear stress, normal/shear creep strain, creep jump, consolidation jump, algorithmic modulus and dissipation. One-dimensional outputs include wall or sensor-equivalent temperatures, mean phase fraction, top displacement, cycle heave, thaw settlement, residual displacement and water change. Two-dimensional fields are plotted on the Delaunay triangulation. Three-dimensional graphics interpolate the axisymmetric field in (r, z) and revolve selected radial shells and a meridional cut plane at the initial, early-freeze, mid-freeze, end-freeze, mid-thaw and end-thaw stages. This is a visualisation of the axisymmetric calculation. VTK export writes points, cells and field arrays for external visualisation. Supplementary Information, Appendix G gives the complete data schema and reproduction commands.

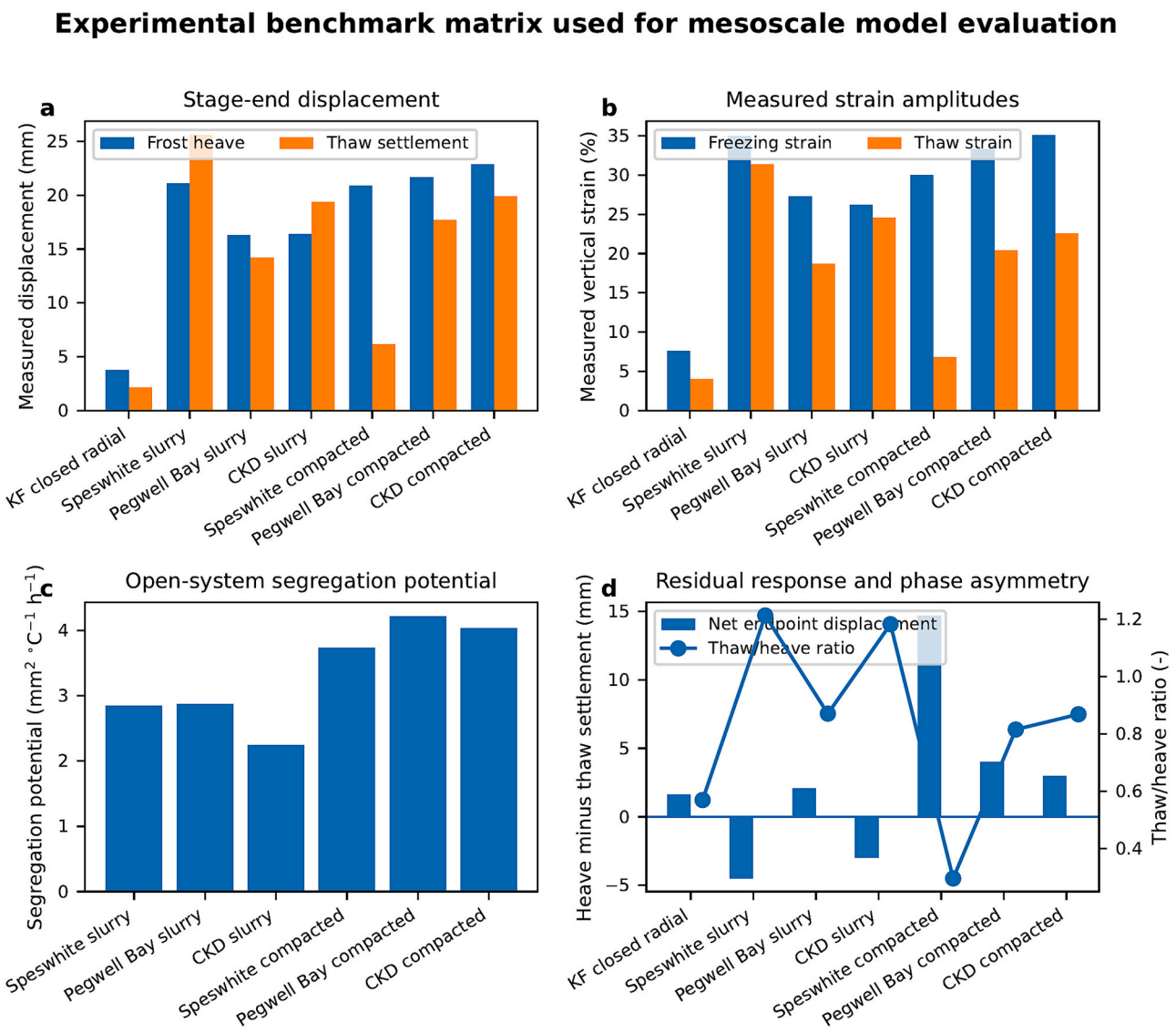

Fig. 4. Experimental benchmark matrix. (a) Measured frost heave and thaw settlement; (b) measured freezing and thaw strains; (c) segregation potential for the six open-system cases; and (d) net endpoint displacement and thaw/heave ratio. The plots use source-reported scalar endpoints and do not fabricate continuous experimental histories.

3. Results

3.1. Experimental materials, test matrix and measured response

The numerical study is anchored to two complementary laboratory programmes rather than to a single homogeneous dataset. The Kieler Förde (KF) programme provides an externally cooled, closed-system marine-clay specimen subjected to 11 radial freeze–thaw cycles under 25 kPa. The independent Cardiff programme provides six open-system, top-down freezing tests on Speswhite kaolin (SK), Pegwell Bay soil (PB) and cement kiln dust (CKD), each tested as an initially saturated slurry and as a compacted specimen under 2 kPa (Al-Hussaini, 2017). The four materials span markedly different grading, plasticity, mineralogy, initial density and hydraulic response (Table 2), while the seven configurations span closed/open drainage, radial/vertical thermal forcing, one/eleven cycles and loose/compacted initial states (Table 3).

The measured response is summarized in Table 4 and Fig. 4. KF produced the smallest first-cycle heave (3.78 mm) and thaw settlement (2.155 mm), under the closed, no-inflow boundary condition. The six open-system specimens heaved between 16.3 and 22.9 mm. Initial state altered thaw response more strongly than peak heave: SK slurry settled 25.6 mm, whereas compacted SK settled only 6.2 mm despite similar heave. PB and CKD compacted specimens exhibited greater heave and segregation potential than their slurry counterparts. The net endpoint response also changed sign: SK and CKD slurries ended below their pre-freezing heights, whereas PB slurry and all compacted cases retained positive residual heave. These observations define the displacement response classes used in calibration; they are not treated as a controlled soil-only comparison because geometry, stress, drainage and thermal schedules differ between KF and the open-system tests.

3.2. Model setup, initial mesh and staged calculation

Fig. 2 documents the complete setup before any calibration result is considered. The selected meshes contained 143 nodes, 218 triangles and 360 Delaunay edges for every case; geometry changed through R and H, but the target topology and random seed were held constant. The Delaunay graph supplies two mechanical modes on every edge, whereas the Voronoi/circumcentric dual supplies heat and water storage/flux measures. This avoids projecting the transport solution between unrelated meshes. The initial preload solution is stored as the zero-displacement reference, so subsequent heave and settlement exclude

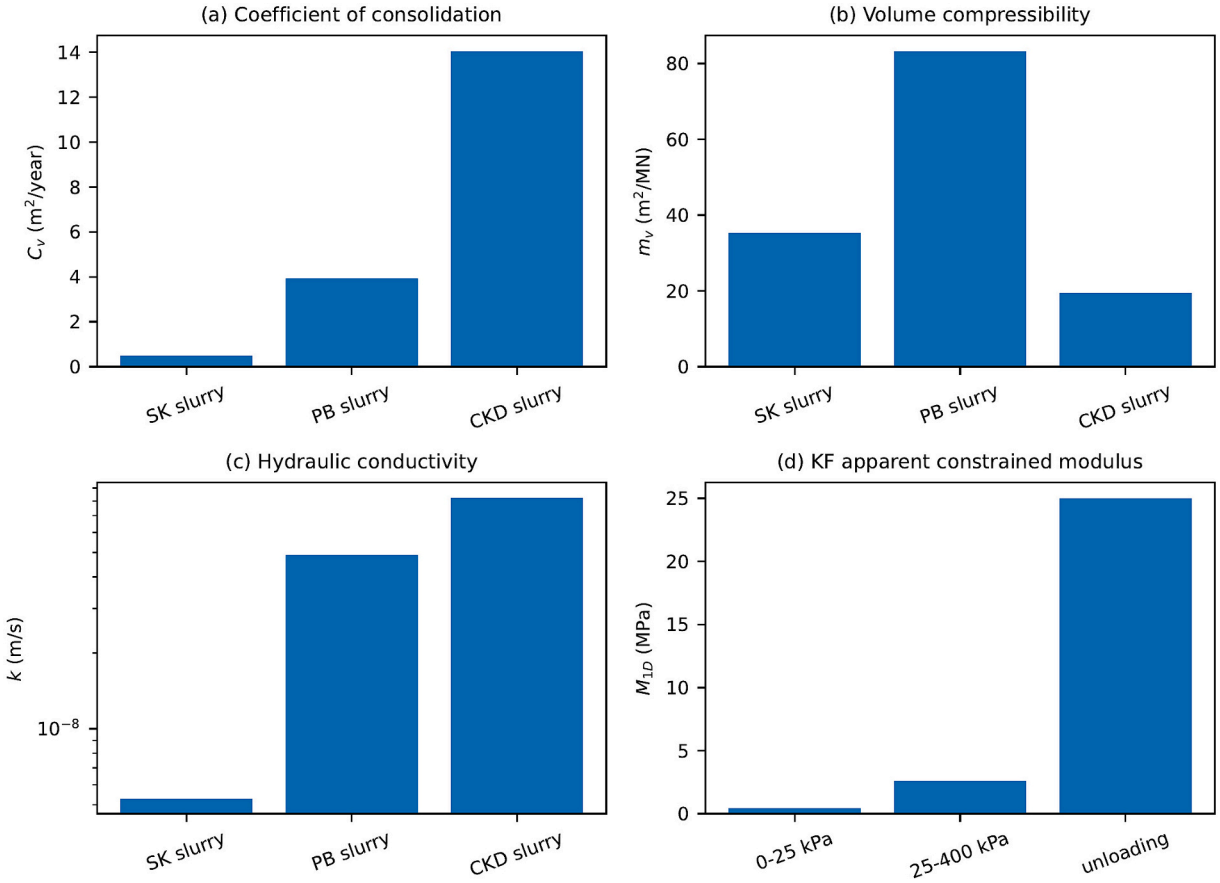

Fig. 5. Consolidation-related parameters. (a) coefficient of consolidation; (b) coefficient of volume compressibility; (c) hydraulic conductivity for the slurry tests; and (d) KF apparent constrained modulus over loading and unloading intervals. The KF flow result was not converted to hydraulic conductivity because the complete hydraulic gradient was unavailable.

the purely mechanical seating displacement. (See Fig. 3.) (See Fig. 8.)

The boundary-condition change between the two programmes is explicit. KF uses a no-flow cylinder with outer-wall thermal exchange, rigid radial confinement and 25 kPa top load. The six Cardiff configurations use an insulated cylindrical wall, top cooling, a warm/open basal reservoir and 2 kPa top load. The same input schema changes only geometry, boundary tags, schedule and material/state records. At every time step, each edge returns a FEAP-format residual and tangent; local creep and consolidation jumps are stored in the edge history. The six reporting stages were selected before plotting and were therefore identical in normalized cycle position for all cases.

3.3. Consolidation, compressibility and available mechanical information

The calculated and source-derived consolidation quantities are summarized in Table 5 and Fig. 5. For the slurry specimens, the source values give $C_v = 0.497$, 3.921 and 14.04 m^2 year^{-1} for SK, PB and CKD. Their corresponding m_v values are 35.38, 83.23 and 19.46 m^2 MN^{-1}, so the apparent one-dimensional moduli are only 0.0283, 0.0120 and 0.0514 MPa. PB is therefore the most compressible under the low-stress consolidation test despite having a larger C_v than SK. CKD combines the largest C_v and hydraulic conductivity with the highest slurry constrained modulus. The indicative Π_c values are 2.68, 0.331 and 0.102; only SK slurry has a characteristic consolidation time longer than the scheduled thaw stage under this screening definition.

The KF loading curve is markedly nonlinear. The secant constrained modulus increases from 0.455 MPa over 0–25 kPa to 2.602 MPa over 25–400 kPa. The 0.3 mm rebound gives an apparent unloading modulus of 25.0 MPa, indicating that most of the total strain accumulated during loading was irreversible. These values constrain lattice stiffness and thaw-consolidation capacity. They do not define shear or tensile strength. Because no triaxial, direct-shear, unconfined-compression or frozen creep-failure tests were supplied, model strength parameters remain priors and no experimentally validated strength calculation is claimed.

3.4. Analytical verification, convergence and backend consistency

The radial-conduction benchmark compared centre temperature in a cylinder against the analytical Bessel-series solution. At the final time, the relative L_2 error was 1.45%; the maximum centre-temperature error over the transient was 5.23 °C, occurring early when the imposed boundary changed most rapidly. The one-phase Stefan test gave a relative front-position root-mean-square error of 3.53% and a maximum absolute error of 3.38 mm. The confined-compression benchmark compared the lattice displacement with an analytical constrained-modulus solution and gave a relative error of 5.88%. These three tests isolate the thermal, phase and mechanical operators before coupled calibration.

Mesh and time-step refinement changed the KF first-cycle heave from 3.737 to 3.894 mm and thaw settlement from 2.085 to 2.232 mm as the mesh increased from 83 to 199 nodes and the time step decreased from 600 to 180 s. The 143-node, 300 s case gave 3.841 mm heave and 2.146 mm thaw settlement and was selected as the principal balance between resolution and runtime. The convergence sequence is not strictly monotonic because random lattice geometry and time-step refinement were changed together; however, all four heave values lie within 4.2% of the finest value and the selected case lies within 1.4%.

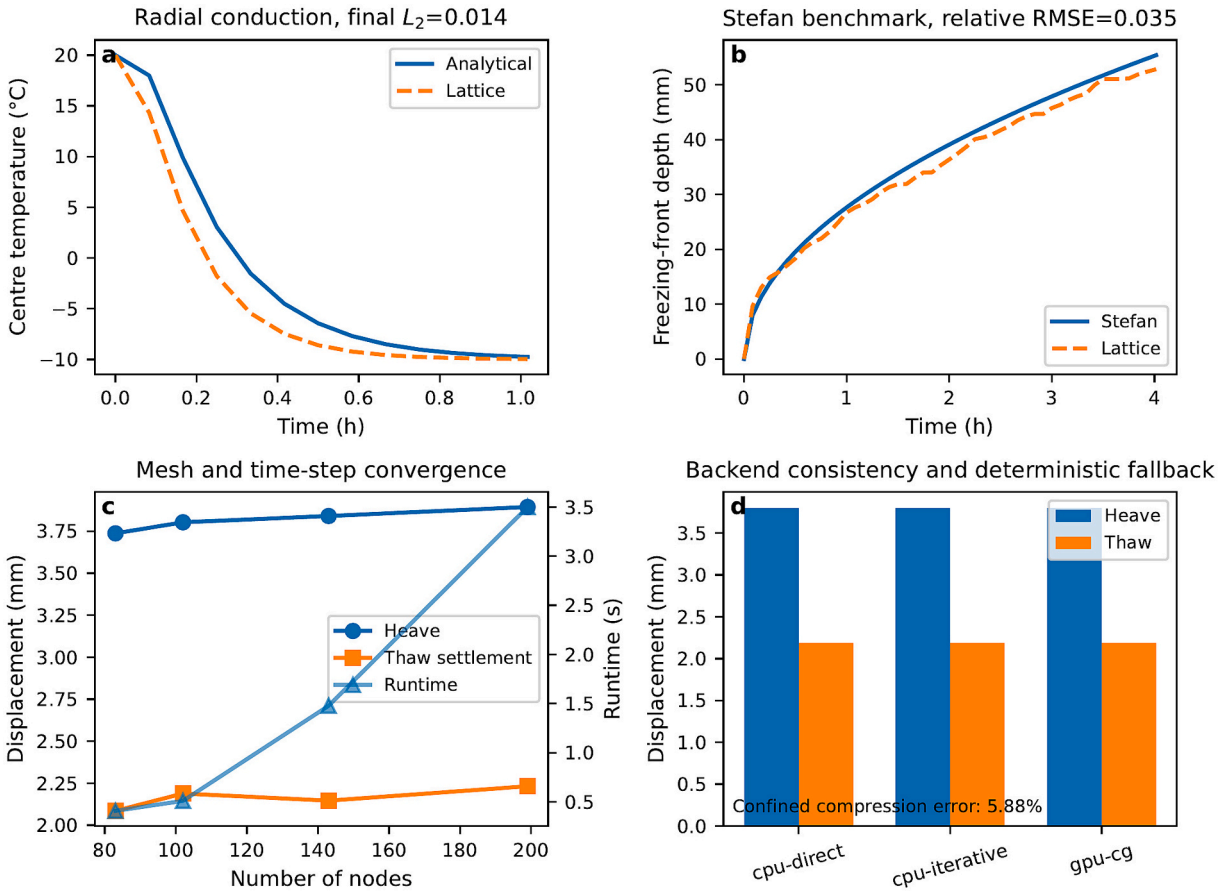

Fig. 6. Numerical verification and consistency. (a) Radial heat-conduction solution; (b) Stefan-front propagation; (c) mesh/time-step sequence and runtime; and (d) agreement of CPU-direct, CPU-iterative and GPU-requested/CPU-fallback calculations.

CPU-direct and preconditioned CPU-conjugate-gradient solutions were numerically indistinguishable at the reported precision. For the test mesh, heave differed by 2.63×10^{-9} mm and thaw settlement by 1.97×10^{-8} mm. A GPU-CG run was requested, but CuPy and a compatible device were unavailable; the code recorded this condition and fell back to the CPU iterative solver, reproducing the same result. Fig. 6 therefore documents implemented backend logic and deterministic fallback, not measured GPU acceleration.

3.5. *Case-level calibration and first-cycle benchmark reproduction*

Supplementary Table S5 and Fig. 7 compare measured and simulated first-cycle endpoints. The combined mean absolute percentage error for the 14 heave and thaw-settlement values was 0.52%, the median was 0.36%, and the maximum was 1.60%. Mean absolute displacement error was 0.071 mm. Heave error averaged 0.45%, whereas thaw-settlement error averaged 0.60%. These small errors demonstrate close reproduction of the calibrated displacement endpoints under both boundary configurations; they do not independently validate the predicted internal water, pressure or phase fields.

The contrast among the measured displacement endpoints is physically informative, but it does not uniquely identify the internal mechanism. KF developed only 3.78 mm measured heave under closed drainage and 25 kPa surcharge, while the open thesis specimens developed 16.3–22.9 mm under 2 kPa. The open-system cases permit basal water supply and use a 24-h top-freezing stage, whereas KF contains only the water initially present in the specimen and is thermally forced around the outer wall. Initial fabric also mattered. Compacted PB and CKD heaved more than their slurry counterparts, whereas SK heave was similar in both states but the compacted SK thaw settlement was much smaller. The model reproduced those endpoint classes after changing source-supported geometry, initial state, drainage and surcharge and calibrating the unmeasured coefficients for each case. The predicted water redistribution is therefore one admissible explanation under the imposed boundaries, not a uniquely established mechanism.

The one-dimensional histories in Fig. 7 show that equal endpoint accuracy does not imply identical transient mechanisms. Open cases exhibit rapid heave growth during the freezing stage and substantial downward motion during thaw. KF responds more slowly and retains a smaller cycle amplitude. The open histories are generated by an imposed top thermal exchange, a warm bottom and a basal water-content boundary; the closed history is generated by outer-wall exchange and no water boundary. Experimental symbols are stage-end values, not fabricated continuous traces. Full time-series RMSE and correlation coefficients are therefore not reported.

The complete numerical values, including freezing and thaw strains, are listed in Supplementary Table S5. Keeping the detailed matrix in the Supplementary Information preserves the main-paper display-item limit while retaining a complete audit trail for every source endpoint and calculated error.

3.6. *FEAP-compatible jump–creep enrichment*

The reduced benchmark model was first retained to preserve the original calibration audit. The new FEAP-compatible model was then run for one complete cycle in every configuration using the same thermal, water and geometry parameters, with thaw densification recast as a local consolidation jump and the temperature-dependent creep law activated. No endpoint-specific re-optimisation was performed. Table 6 shows that the enriched model retained a median endpoint APE of

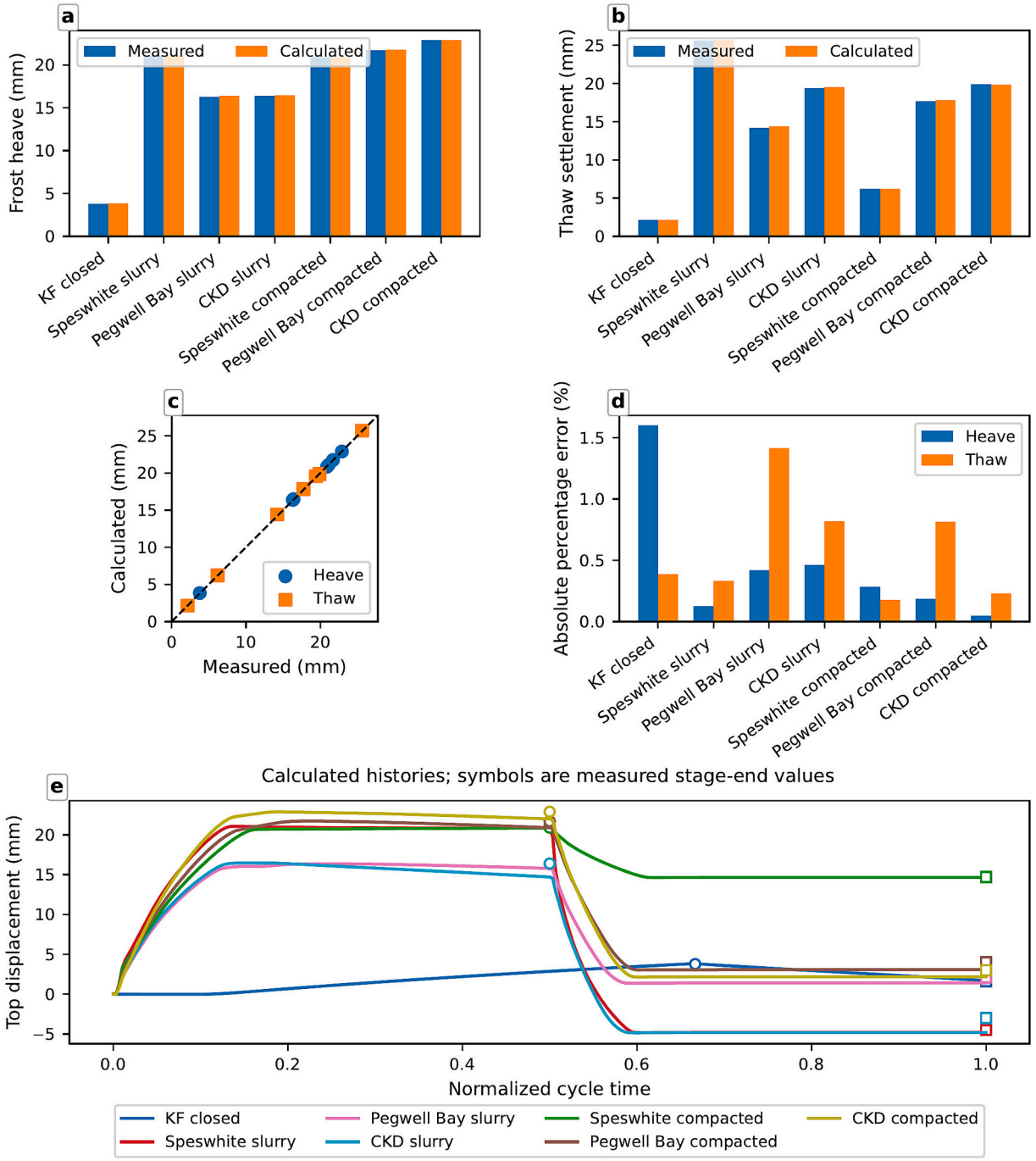

Fig. 7. One-dimensional benchmark reproduction. (a) Frost heave; (b) thaw settlement; (c) measured–simulated parity; (d) absolute percentage errors; and (e) simulated first-cycle histories with measured freezing and thaw-stage endpoint symbols.

3.03%, a mean of 3.39% and a maximum of 8.84%. The mean dimensional endpoint error was 0.567 mm. The enhanced calculation is therefore less tightly fitted than the reduced benchmark, but all endpoint differences remain below 9% while the irreversible mechanisms are separated explicitly.

The bond-scale decomposition is revealing. Maximum normal creep jumps were 0.23–2.93 μm, whereas consolidation jumps ranged from zero to 3.76 mm. Thus, the short freeze–thaw schedules do not generate large creep deformation under the restrained literature priors; most irreversible movement is attributed to thaw consolidation. SK slurry develops the largest consolidation jump and the largest measured thaw settlement. Compacted SK develops essentially no additional consolidation jump in the enriched preset and retains the smallest measured thaw settlement among the open cases. PB and CKD states occupy the intermediate range. This ranking was not imposed through a common strength value; it follows the state-specific consolidation capacity and measured endpoint constraints.

The one-cycle CPU-direct runtimes were 1.15–13.52 s on the archived execution host. The FEAP-style kernel required one residual/tangent assembly and sparse solve per staggered step in the production route, and the mean reported mechanical iteration count was one. The larger reported “utilization” values in the raw diagnostic file are not interpreted as failure because the bond strengths are uncalibrated priors; they are retained only to identify where independent strength testing would be required.

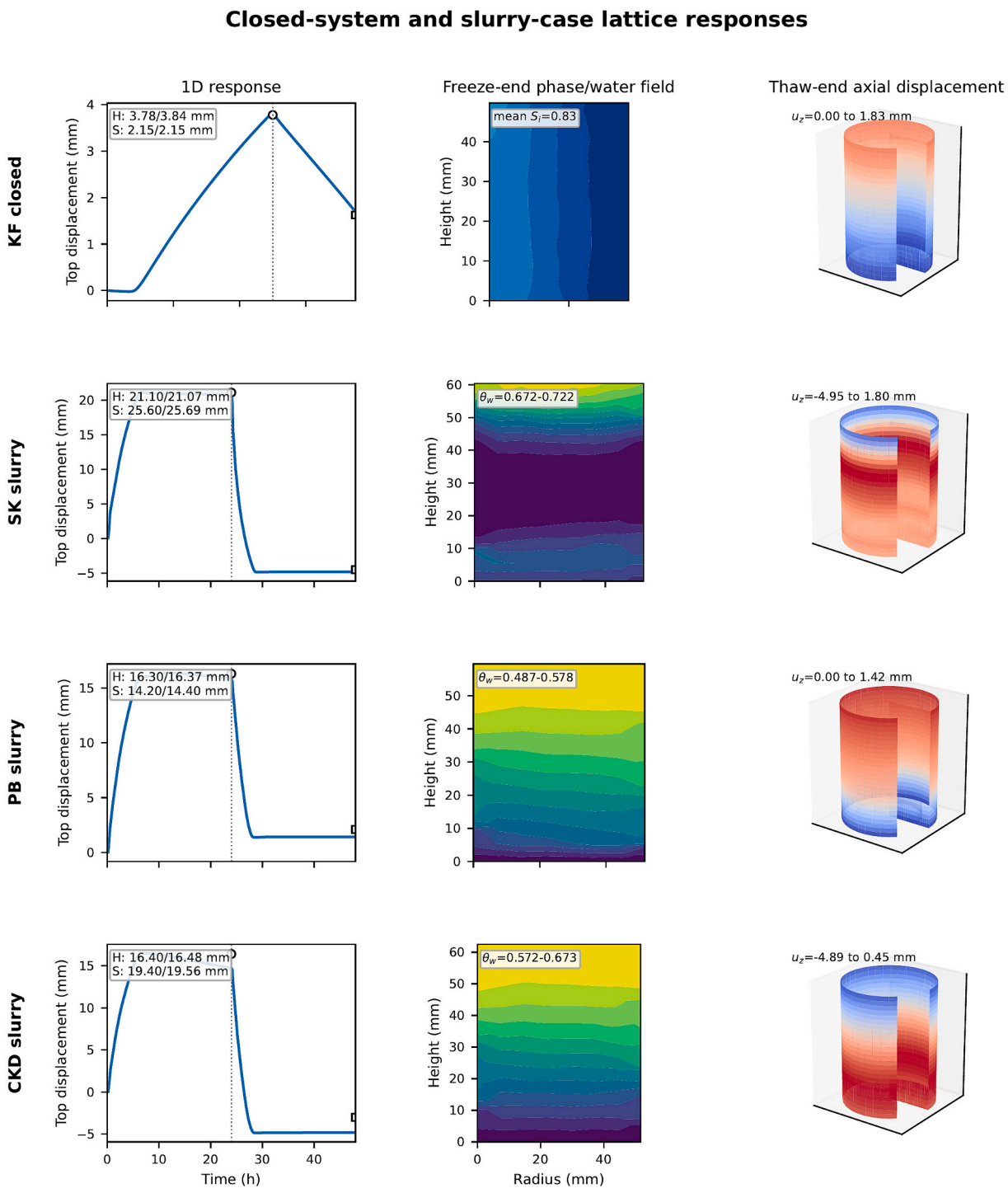

Fig. 9. Closed-system and slurry-case lattice simulations. Each row gives the simulated first-cycle vertical displacement with measured freezing and thaw-stage endpoints, the freeze-end ice fraction or total-water field, and the thaw-end axial-displacement field revolved about the symmetry axis. Values in the left-panel boxes are experiment/simulation pairs for heave (*H*) and thaw settlement (*S*).

3.7. Case-specific lattice response

Figs. 9 and 10 provide a common 1D–2D–3D view of every calibrated benchmark configuration. The left column shows simulated vertical displacement together with the measured freezing and thaw-stage endpoints. The centre column shows the freeze-end internal field most diagnostic of the boundary condition: ice fraction for the closed KF case and total-water redistribution for the open cases. The right column shows the thaw-end axial-displacement field revolved about the symmetry axis. The revolved views are post-processing of the two-dimensional axisymmetric solution, not independent three-dimensional calculations. Full-resolution histories and fields are supplied as Supplementary Figs. S1–S21.

For clarity, “thaw settlement” denotes the maximum downward change from the freeze-end displacement to the minimum displacement reached during thaw. “Final residual displacement” denotes the top displacement at the end of the scheduled thaw stage. These quantities need not equal heave minus thaw settlement because several open-

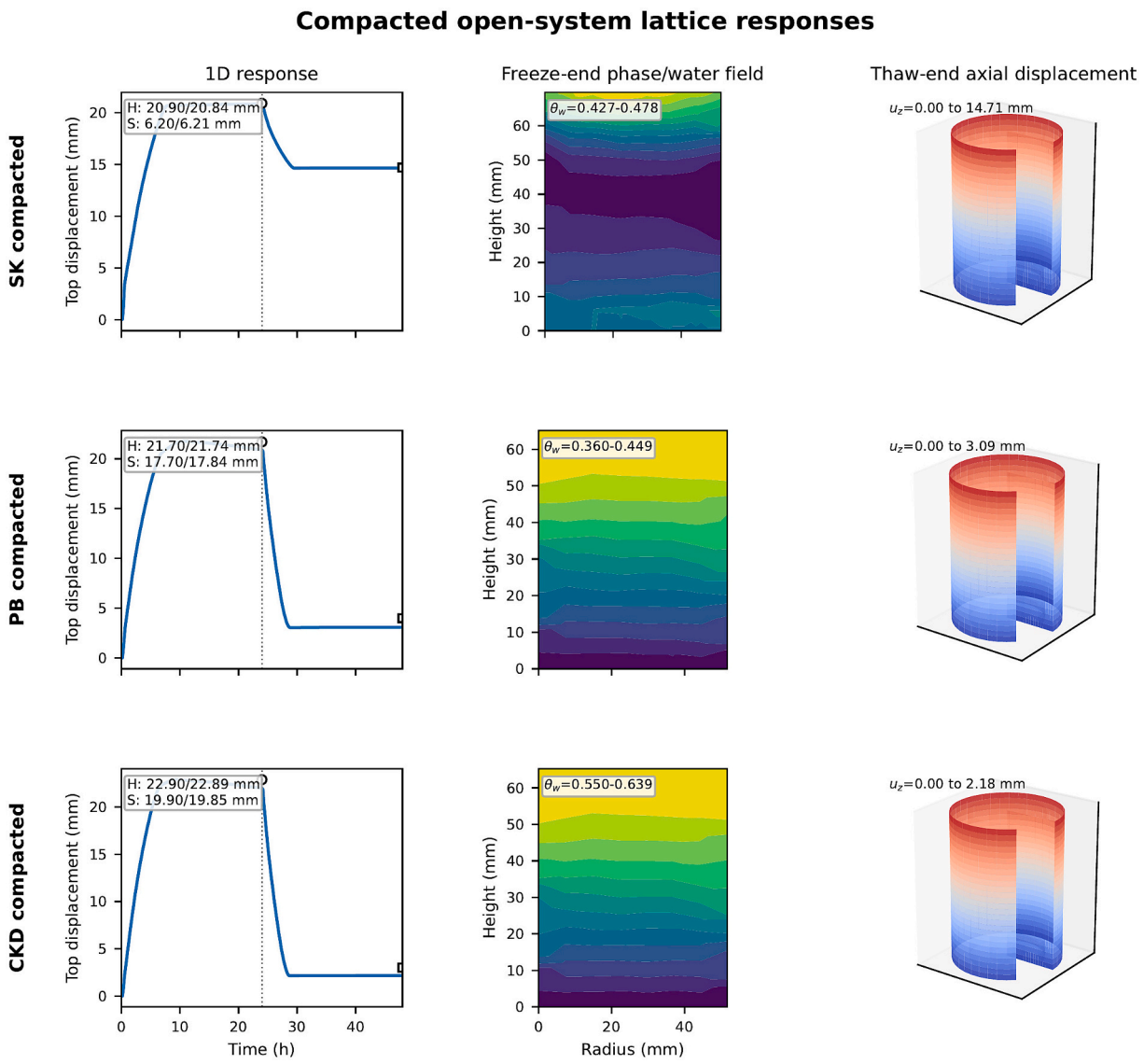

Fig. 10. Compacted open-system lattice simulations. Each row gives the simulated first-cycle vertical displacement with measured freezing and thaw-stage endpoints, the freeze-end total-water field, and the thaw-end axial-displacement field revolved about the symmetry axis. Values in the left-panel boxes are experiment/simulation pairs for heave (H) and thaw settlement (S).

system calculations show a small late-thaw rebound.

3.7.1. *Kieler Förde closed outer-wall case*

The KF calculation reproduced the measured 3.78 mm first-cycle heave with 3.841 mm and the inferred 2.1546 mm thaw settlement with 2.146 mm. The final residual top displacement was +1.694 mm. The phase field develops from the outer wall toward the axis, producing an annular frozen region that differs fundamentally from the vertical fronts in the open columns. Because all hydraulic boundaries are closed, calculated external water intake is numerically negligible and total water remains nearly uniform (θ_w = 0.374998–0.375283). Deformation is generated by in-pore phase expansion, thermal strain and the bounded cyclic state variables. The residual upward displacement and subsequent reduction in incremental response are consistent with the reported multi-cycle stabilisation, although the earliest heave rate remains underpredicted.

3.7.2. *Speswhite kaolin slurry*

The initially saturated SK slurry developed the largest measured thaw settlement in the seven-case set: 25.6 mm, exceeding its 21.1 mm frost heave. The simulation gave 25.685 mm settlement and 21.074 mm heave. Freeze-end total water ranged from 0.672 to 0.722 and concentrated toward the top-down freezing zone. The final residual top displacement was −4.799 mm, confirming a net contractive cycle. This response is compatible with the high initial void ratio and very high clay fraction of the slurry, but the internal water field remains a model prediction because only post-stage water-content sections were available for comparison (Al-Hussaini, 2017).

3.7.3. *Pegwell Bay slurry*

The PB slurry produced lower heave and settlement than the SK slurry. Measured values of 16.3 mm and 14.2 mm were reproduced as 16.368 mm and 14.401 mm. The freeze-end water field ranged from 0.487 to 0.578 and increased toward the upper frozen region. The final residual top displacement was +1.408 mm. The calibrated result illustrates that the same transport and lattice operators can reproduce a different endpoint response after changing the measured initial state, geometry and case coefficients rather than the governing algorithm; it does not independently validate the predicted internal water field.

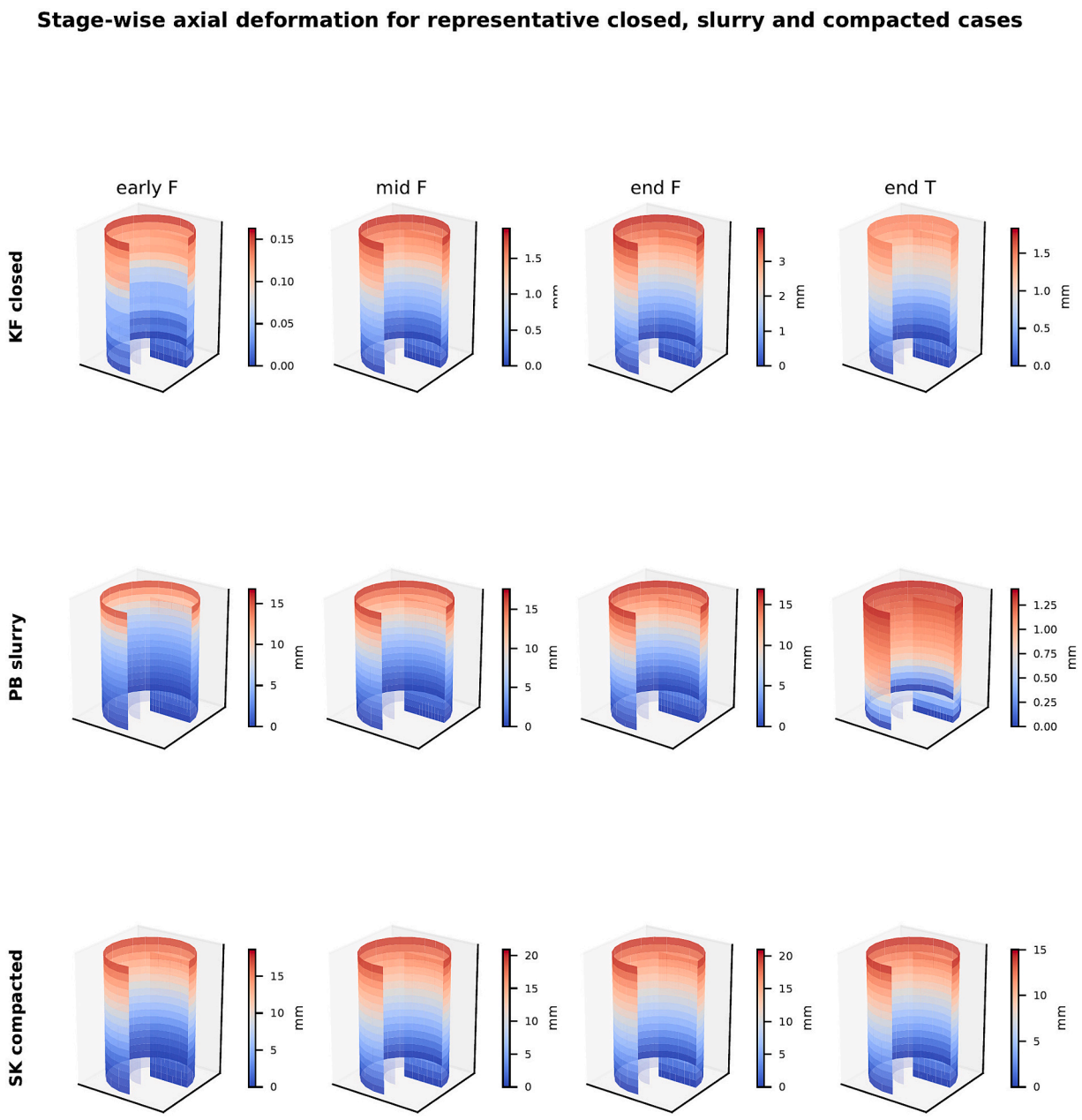

Fig. 11. Representative stage-wise axial-displacement fields from the FEAP jump–creep model: closed KF, PB slurry and compacted SK at early freezing, mid freezing, end freezing and end thaw. Each cutaway cylinder is a revolution of the two-dimensional axisymmetric field. Complete six-stage temperature, ice-fraction, displacement and inelastic-jump atlases for every case are provided in the Supplementary Information.

3.7.4. Cement kiln dust slurry

The CKD slurry had measured heave close to PB slurry (16.4 mm) but a larger thaw settlement of 19.4 mm. Corresponding simulations were 16.476 mm and 19.559 mm. Total water ranged from 0.572 to 0.673 at freeze end, and the final residual displacement was −4.825 mm. The negative residual is therefore not controlled by frost heave alone; in the reduced model it emerges from the combination of open-system water redistribution and the thaw-densification state variable. Because CKD is cementitious and its microstructure can evolve chemically, this agreement should be interpreted as apparatus-scale endpoint reproduction rather than proof of a unique constitutive mechanism.

3.7.5. Speswhite kaolin compacted

Compacted SK heaved almost as much as the slurry (20.9 mm measured and 20.841 mm simulated), but its measured thaw settlement fell to 6.2 mm; the calculation gave 6.211 mm. Freeze-end total water ranged from 0.427 to 0.478. The final residual top displacement of +14.662 mm was the largest positive residual among all cases. The contrast between the two SK states is one of the strongest tests of initial-condition transfer in the dataset: mineralogy is unchanged, whereas void ratio, dry unit weight and preparation history differ. The lattice reproduces the contrast through state-dependent stiffness, water storage and bounded irreversible strain rather than through a different mesh topology.

3.7.6. Pegwell Bay compacted

Compacted PB developed 21.7 mm heave and 17.7 mm settlement, reproduced as 21.740 mm and 17.844 mm. Freeze-end total water ranged from 0.360 to 0.449, and the final residual top displacement was +3.074 mm. Both measured endpoint quantities exceed those of the PB slurry, consistent with the thesis observation that compacted PB had a higher segregation potential under the imposed test conditions (Al-

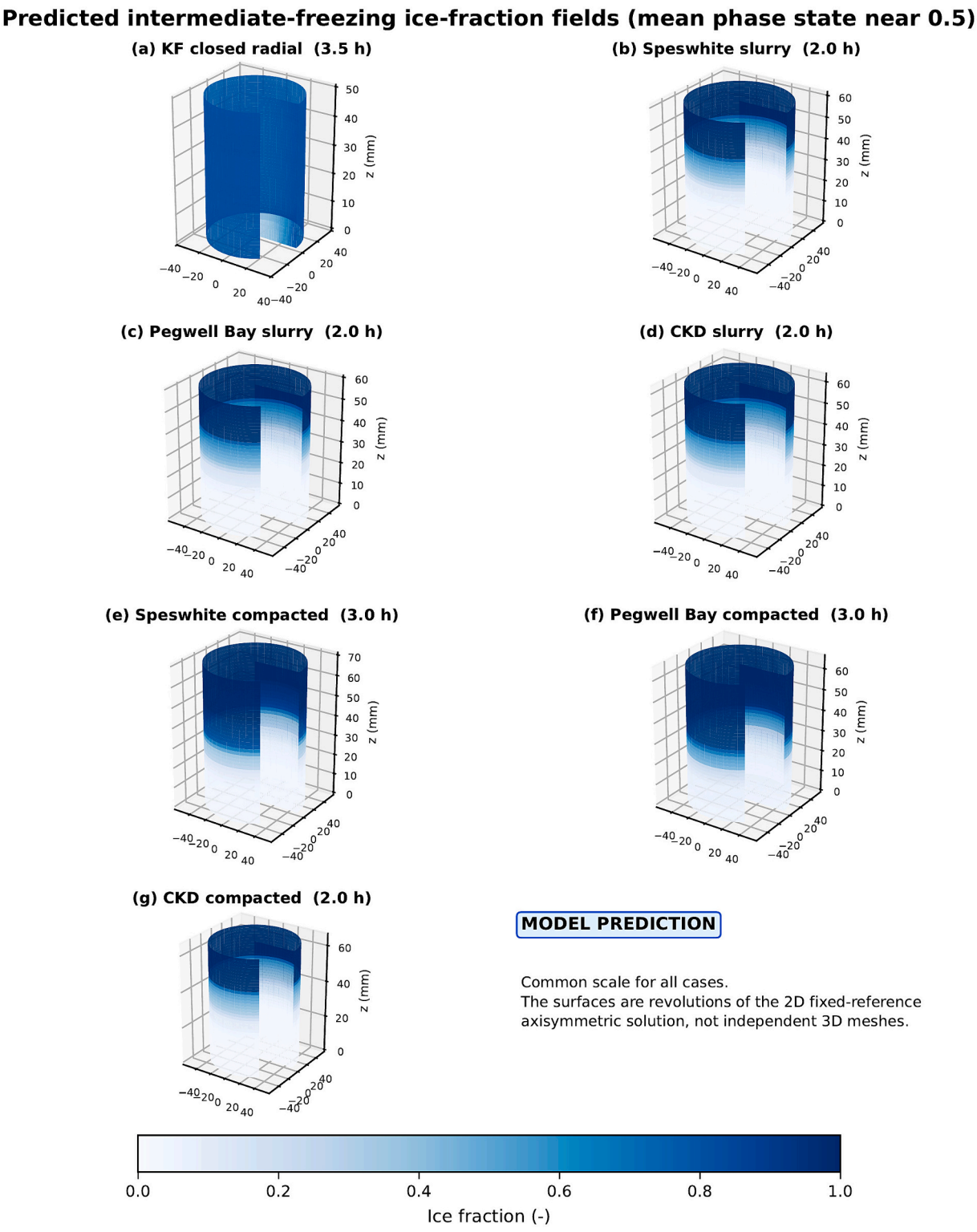

Fig. 12. Predicted intermediate-freezing ice-fraction fields for all seven configurations. For each case, the displayed snapshot has domain-mean ice fraction closest to 0.5; elapsed times are given in the panel titles. Each panel is a revolution of the fixed-reference two-dimensional axisymmetric solution, with nested cylindrical shells and a meridional cut plane. A common 0–1 colour scale is used. The fields were not independently validated against measured freezing-front positions and are not independent three-dimensional meshes.

Hussaini, 2017). The predicted water and displacement fields show that the larger response is distributed through the specimen rather than being represented as a single imposed top displacement.

3.7.7. Cement kiln dust compacted

Compacted CKD produced the largest frost heave in the primary dataset: 22.9 mm measured and 22.889 mm simulated. Thaw settlement was also large (19.9 mm measured and 19.855 mm simulated). Freeze-end total water ranged from 0.550 to 0.639. The final residual top

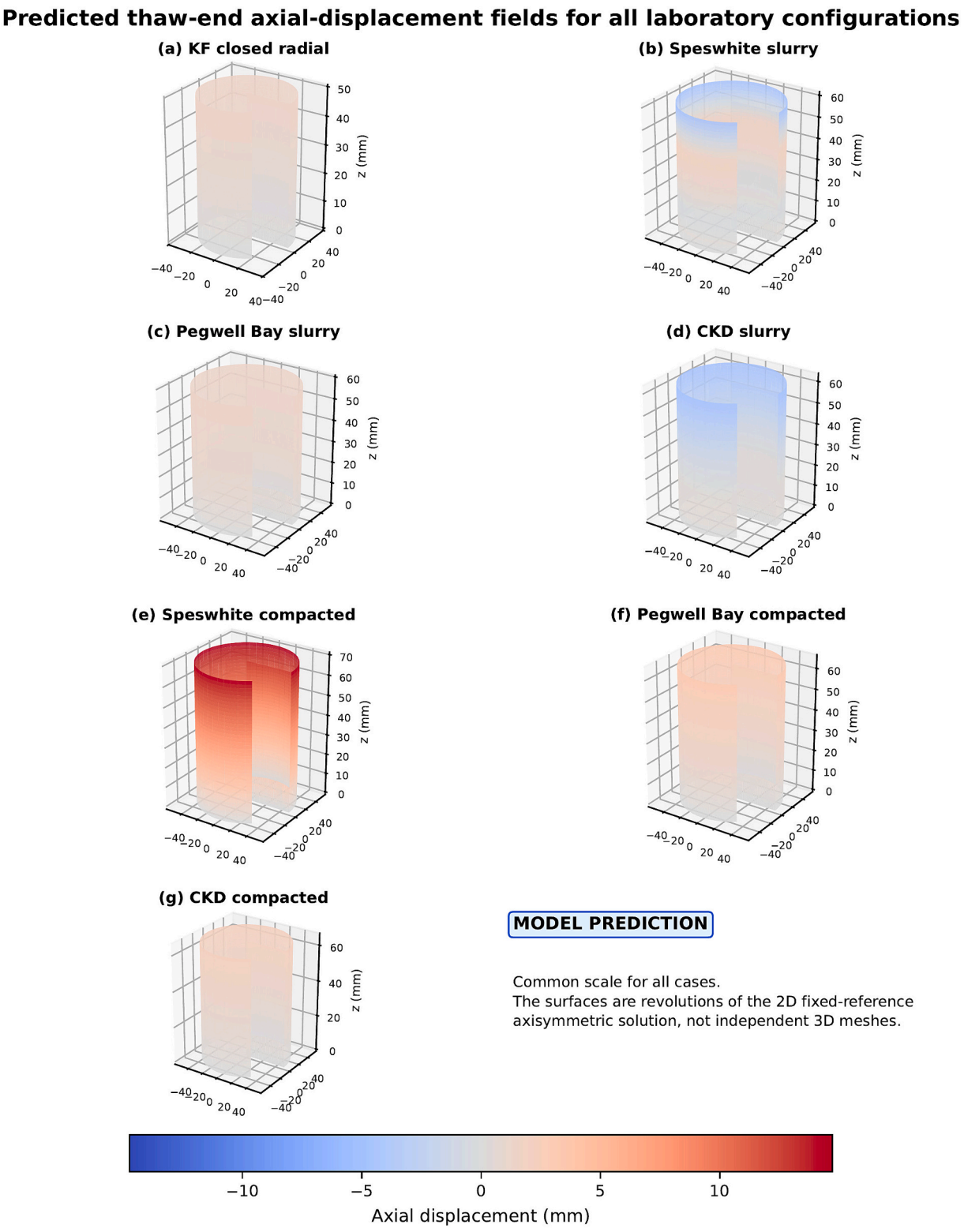

Fig. 13. Predicted thaw-end axial-displacement fields for all seven configurations. A clear common symmetric colour scale permits direct comparison of residual expansion and contraction. The surfaces are revolutions of the fixed-reference axisymmetric solution; for cases with large measured axial strain they are reduced-order displacement visualisations rather than finite-strain calculations.

displacement was +2.170 mm. Among the open cases, the reduced transport calculation predicted the largest freeze-stage water intake for this preset. That quantity is useful for comparing numerical cases but is not an independently validated measurement. Together, the CKD slurry and compacted results show that similar heave can coexist with different residual states and that settlement must be treated as a separate calibration and interpretation target.

Across all cases, the field plots support the numerical narrative but do not prove field uniqueness. The endpoint calibration constrains the integrated vertical response, while temperature, water, cryosuction,

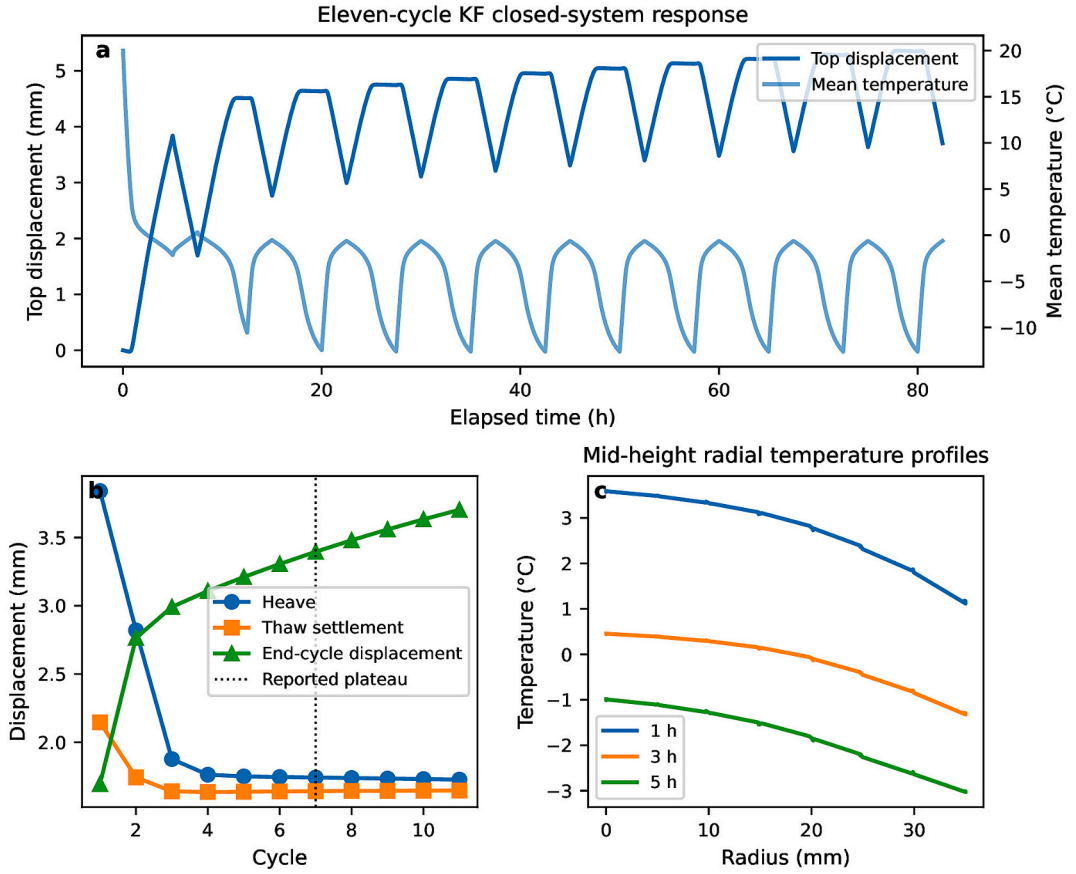

Fig. 14. Cyclic KF simulation. (a) Eleven-cycle displacement and mean-temperature history; (b) cycle heave, thaw settlement and end-cycle displacement with the reported plateau near cycle 7; and (c) mid-height radial temperature profiles during the first freezing branch.

bond stress and displacement distributions depend on parameters that were not measured for every material. Supplementary Table S8 therefore reports these internal quantities explicitly as simulated diagnostics, separate from the source-derived calibration or trend-assessment targets.

3.8. Stage-wise three-dimensional freezing and thawing response

Fig. 11 summarizes four stages for representative closed, slurry and compacted cases, while Supplementary stage atlases provide initial, early-freeze, mid-freeze, end-freeze, mid-thaw and end-thaw temperature, ice fraction, axial displacement and inelastic-jump fields for all seven cases. The graphics are revolved views of the two-dimensional axisymmetric solution; the FEAP edge calculations remain in the meridional plane.

KF develops an outside-in temperature gradient. The outer annulus cools first, the ice-fraction contour advances radially toward the axis, and axial heave develops through the thickness under radial confinement. Because the hydraulic boundaries are closed, the inelastic-jump row remains small and the end-thaw residual is controlled mainly by phase recovery and the bounded cyclic consolidation variable. This is qualitatively distinct from every open-system column.

The three slurry cases develop a vertical front from the cooled top. In SK slurry, the high initial void ratio and low C_v delay consolidation relative to thaw; the inelastic jump grows strongly during melting and produces net contraction. PB slurry has the largest m_v but a faster consolidation coefficient, so its local consolidation jump is moderate and the specimen retains a small positive residual. CKD slurry has the largest C_v and k of the slurry set; water and temperature redistribute rapidly, yet its calibrated thaw capacity produces a larger contraction than PB. The stage plots distinguish the corresponding model-predicted field patterns, but the patterns are not independently validated by co-registered internal measurements.

The compacted cases retain positive residual displacement. Compacted SK has almost the same frost heave as SK slurry but much smaller thaw settlement; its stage atlas shows little added consolidation jump and a large remaining axial-expansion field at the end of thaw. Compacted PB and CKD develop intermediate consolidation-jump bands during thaw and residual heaves of the same order. In every case the creep jump remains several orders of magnitude smaller than the specimen-scale displacement, confirming that the short experiments constrain consolidation more strongly than long-term creep.

3.9. Predicted three-dimensional intermediate-freezing phase fields

Fig. 12 compares case-specific intermediate-freezing states rather than equal clock times. For each configuration, the stored snapshot with domain-mean ice fraction closest to 0.5 was selected; this occurred at 3.5 h for KF, 2.0 h for four open-system cases and 3.0 h for compacted SK and PB. The KF prediction develops inward from the externally cooled cylindrical wall and therefore forms an annular phase pattern. The six top-cooled columns develop a vertically advancing transition from the upper boundary. The comparison establishes that the implemented boundary conditions create different numerical phase topologies. It does not establish a measured freezing-front trajectory, because co-registered front-position data were not available for all cases. The snapshots are consequently used to interpret the calculated displacement response and to check implementation consistency, not as independent phase-field validation.

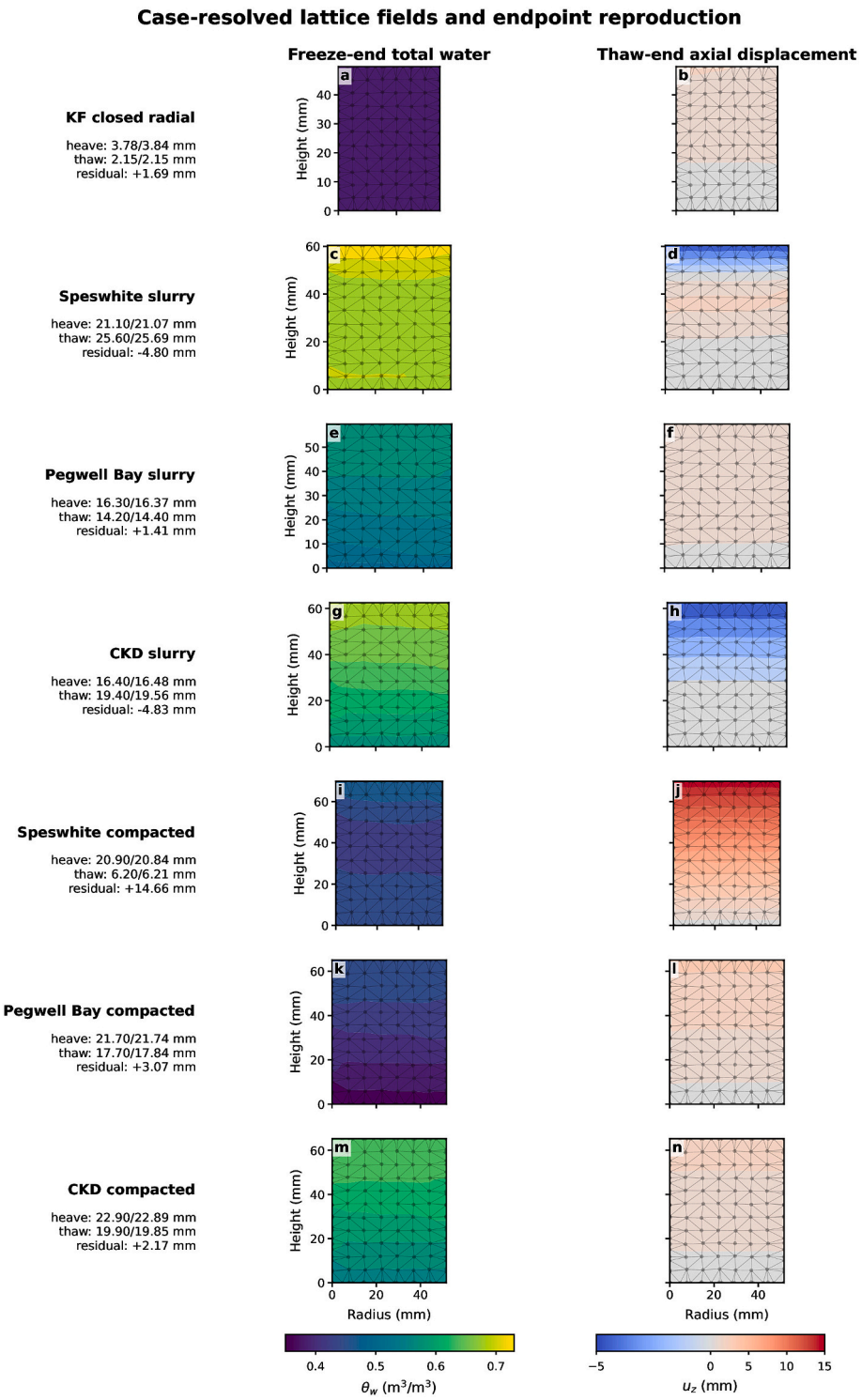

Fig. 15. Common-scale case-resolved lattice fields. For each configuration, the left panel shows freeze-end total volumetric water content and the right panel shows thaw-end axial displacement; Delaunay edges and nodes are overlaid. Text at left gives experimental/simulated heave, experimental/simulated thaw settlement and final simulated residual top displacement. The residual is evaluated at the scheduled end of thaw and can differ from heave minus the maximum thaw settlement because late-stage rebound is retained.

3.10. Mesoscale three-dimensional thaw-end deformation fields

Fig. 13 compares thaw-end axial displacement on a common signed scale. The closed KF specimen retains a low-amplitude positive displacement. SK and CKD slurries contain zones of negative axial displacement after thaw, consistent with net contraction of the measured endpoints, whereas PB slurry remains slightly positive. The compacted specimens retain positive residual heave, with compacted SK showing the largest field amplitude. The cutaway views make clear that the top displacement is the boundary integral of a distributed field: specimens with comparable heave can have different internal gradients and residual states because phase distribution, water access, stiffness and densification history differ. The Supplementary Information provides corresponding three-dimensional ice-fraction and total-water atlases.

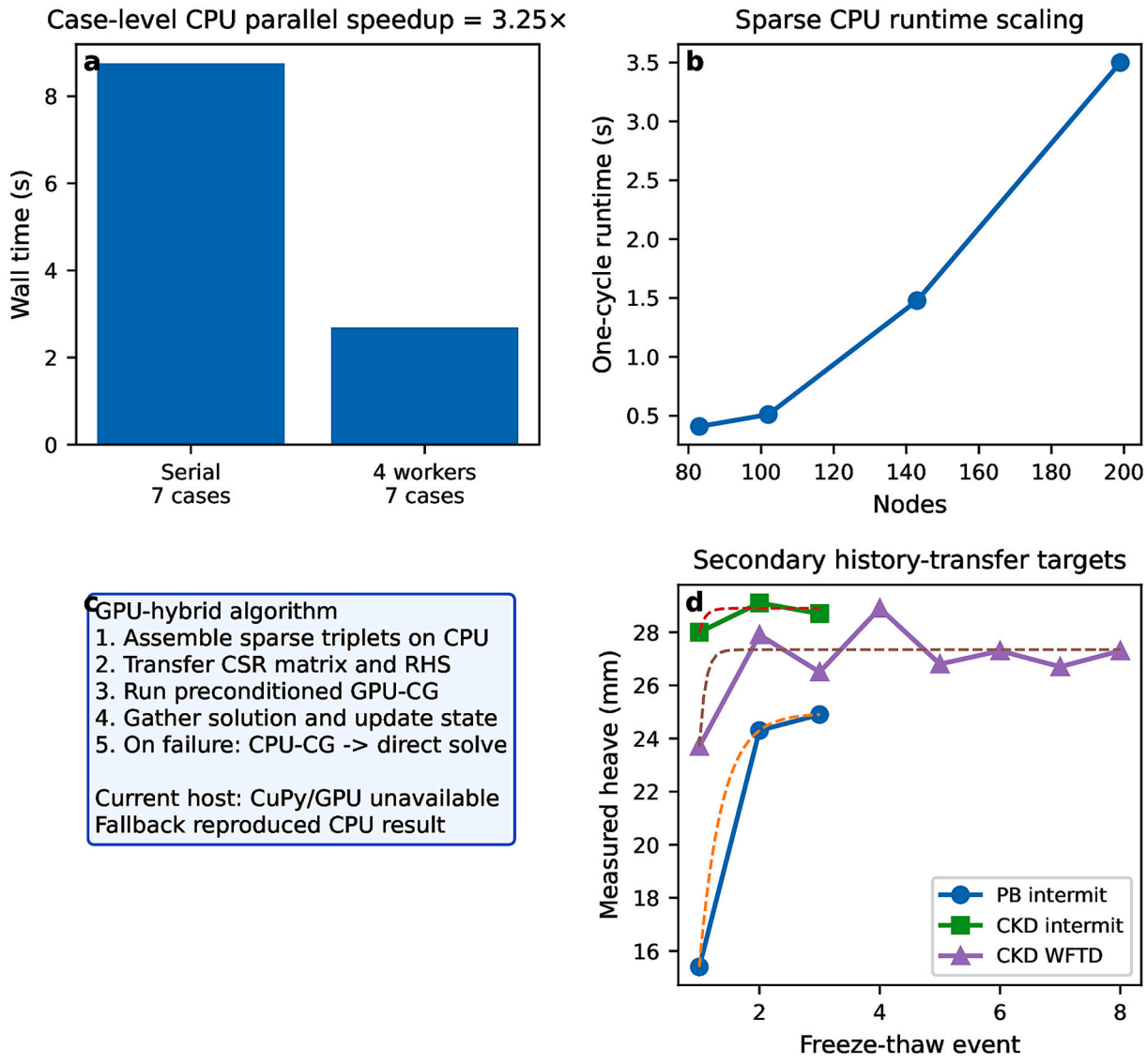

Fig. 16. Computation and transfer. (a) Measured serial and four-worker CPU wall time; (b) one-cycle CPU runtime with mesh size; (c) implemented GPU-hybrid pathway and deterministic fallback; and (d) secondary cyclic laboratory histories retained as future transfer targets.

3.11. *Cyclic KF response*

The full KF computation covered 11 cycles and retained the material state between cycles (Fig. 14). The calculated first-cycle heave was 3.841 mm, freezing strain 7.73%, thaw settlement 2.146 mm, and thaw/freezing ratio 0.559. Corresponding reported values were 3.78 mm, 7.6%, approximately 2.155 mm, and 0.57. The code reached the prescribed freezing and thawing stage durations of 5 and 2.5 h, respectively, because those durations defined the apparatus schedule. The maximum early calculated deformation rate was 1.13 mm h^{-1}, 30.4% lower than the reported 1.62 mm h^{-1} indicator; this is the largest scalar discrepancy and shows that the smooth phase transition and homogeneous bond field do not resolve the earliest transient as accurately as the integrated displacement.

Thaw densification accumulated rapidly in early cycles and approached its bounded limiting state, producing a computed plateau in cycle 6 compared with the reported approximate cycle 7. The one-cycle difference is reasonable at the present level of data resolution but should not be interpreted as an exact prediction because the source figures do not provide a tabulated cycle-by-cycle displacement series. The predicted radial profiles demonstrate the consequence of outside-in forcing: the wall region cools and freezes before the axis, producing a curved radial phase front rather than the vertical front of the open tests. This result directly addresses the actual laboratory boundary condition without claiming that the apparatus reproduces inside-out wellbore heating.

3.12. *Cross-case lattice-field atlas*

Fig. 15 places the seven freeze-end water fields and seven thaw-end axial-displacement fields on common scales and overlays the Delaunay connectivity. This view complements Figs. 9 and 10: those figures provide the complete 1D–2D–3D response by case, whereas the atlas emphasizes direct comparison of the same state variables across materials and preparation conditions. Within the selected reduced transport model, the open cases develop freeze-end total-water ranges of 0.050–0.101, while the closed KF range is less than 3×10^{-4}. This contrast follows from the imposed basal-reservoir and no-flow boundary tags and should be read as a model response, not as independent proof of a unique water-supply mechanism.

The thaw-end fields reveal three residual-response classes. SK and CKD slurries finish with net contractions of 4.799 mm and 4.825 mm; PB

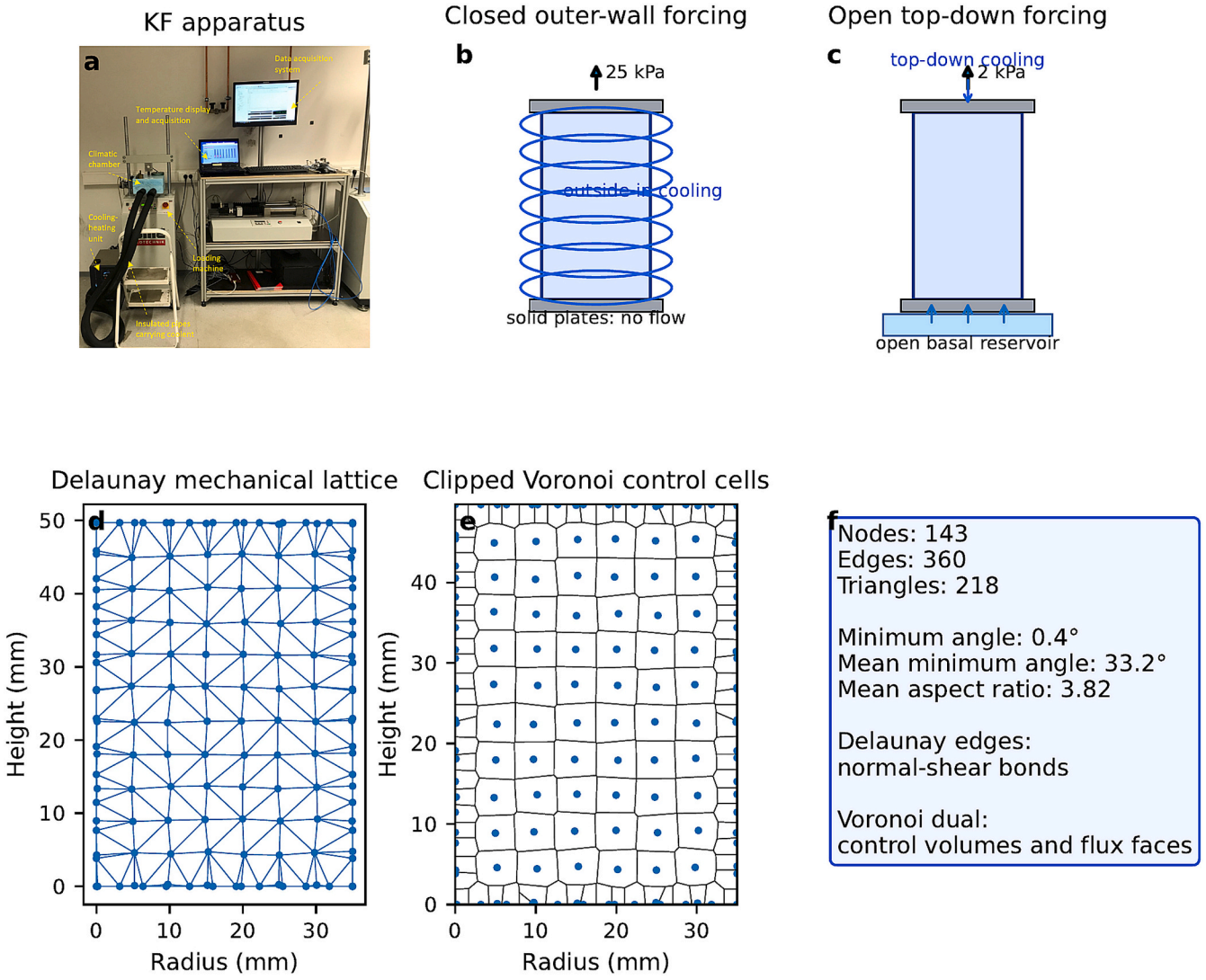

Fig. 3. Laboratory configurations and dual-mesh preprocessing. (a) KF apparatus; (b) closed outside-in thermal forcing and no-flow boundaries; (c) open top-down forcing with a basal reservoir; (d) Delaunay mechanical lattice; (e) clipped Voronoi visualisation; and (f) representative mesh statistics and the distinct roles of the primal and dual geometries.

slurry retains a small positive displacement of 1.408 mm; and all compacted cases retain positive residual heave, led by compacted SK at 14.662 mm. KF remains low-amplitude and water-limited, with a + 1.694 mm residual. Comparable peak heave therefore does not imply comparable post-thaw state. Full temperature, ice, water and displacement panels at both freeze and thaw endpoints, together with revolved three-dimensional views, are supplied in Supplementary Figs. S1–S21.

3.13. CPU parallelism, GPU pathway and transfer to cyclic histories

A measured process-parallel benchmark executed seven coarse one-cycle cases serially and with four CPU workers. Wall time decreased from 8.75 to 2.69 s, giving a speedup of 3.25 (Fig. 16). The speedup is lower than the ideal factor of four because process startup, imports, memory allocation and operating-system scheduling remain serial or duplicated. Within a single case, sparse matrix assembly and time stepping remain sequential in the reference implementation; the most efficient CPU parallelization is therefore across independent materials, calibration candidates, mesh levels or sensitivity cases.

The GPU pathway converts a SciPy CSR matrix and right-hand side to CuPy/cupyx objects, executes conjugate gradients, gathers the solution and records solver metadata. If import, allocation or convergence fails, the code uses preconditioned SciPy CG and then sparse direct factorization. No compatible GPU was available in the execution environment, so no numerical GPU speedup is reported. This negative result is important: GPU capability has been implemented and its fallback verified, but acceleration must be measured on named hardware and at a problem size large enough to overcome transfer overhead. The pseudocode and benchmarking protocol in Methods and Supplementary Information, Appendix F provide the procedure for that test.

The secondary thesis histories demonstrate how the framework can be extended beyond one freeze–thaw cycle. Intermittent PB heave increased from 15.4 to 24.3 and 24.9 mm; intermittent CKD heave remained near 28–29 mm; and CKD wet–freeze–thaw–dry heave fluctuated between 23.7 and 28.9 mm. Saturating response curves fitted to these source values are shown only as transfer targets, not as results of the present base parameter sets. Reproducing wetting and drying requires explicit vapour/evaporation and unsaturated suction laws that lie beyond the current freeze–thaw solver.

4. Discussion

The study demonstrates a complete laboratory-scale modelling chain rather than an isolated constitutive curve fit. Source geometry and

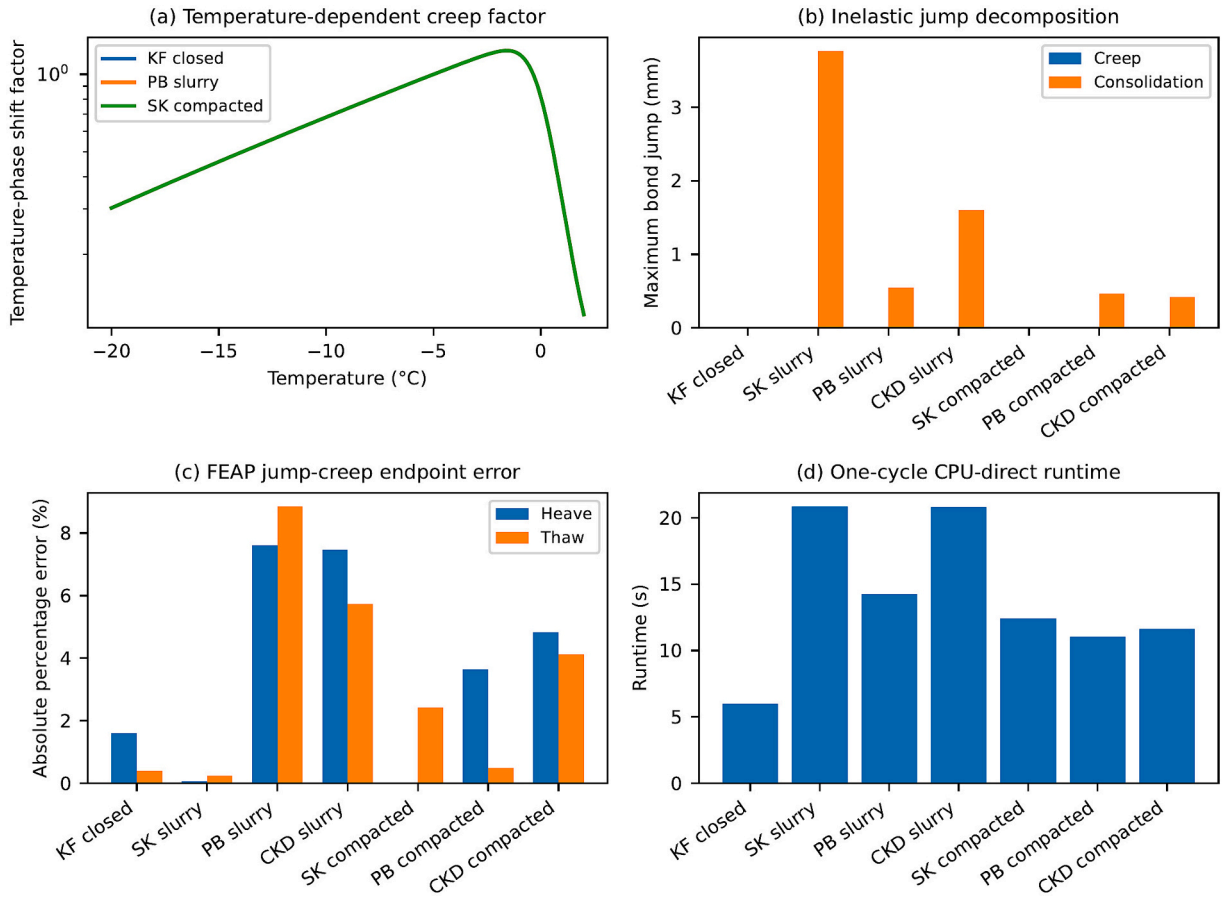

Fig. 8. Temperature-dependent creep and FEAP jump–creep performance. (a) bounded temperature–phase shift factor; (b) maximum creep and consolidation jumps; (c) endpoint errors without re-optimisation; and (d) one-cycle CPU-direct runtime.

Table 5
Consolidation and stiffness information used to constrain the lattice model. Πc = $H^2/(Cv\ tT)$ is an indicative consolidation-to-thaw time ratio. A dash denotes unavailable or inapplicable source information.

Case or stress interval	Cv (m^2 $year^{-1}$)	mv (m^2 MN^{-1})	M1D (MPa)	k (m s^{-1})	Πc
SK slurry, 2 kPa	0.497	35.38	0.0283	5.28×10^{-9}	2.681
PB slurry, 2 kPa	3.921	83.23	0.0120	4.89×10^{-8}	0.331
CKD slurry, 2 kPa	14.04	19.46	0.0514	8.25×10^{-8}	0.102
KF, loading 0–25 kPa	–	2.196	0.455	–	–
KF, loading 25–400 kPa	–	0.384	2.602	–	–
KF, apparent unloading 400–25 kPa	–	0.040	25.000	–	–

boundary conditions are converted into an axisymmetric domain, an irregular point cloud is generated once, Delaunay and Voronoi measures are stored, initial preload is solved, and the same staggered thermal–water–mechanical sequence is executed for closed and open systems. The FEAP-compatible organization makes the mechanical implementation auditable: each edge returns a residual and tangent, while local jump and creep histories are updated in a small constitutive routine. This division between preprocessing, element calculation, global solution and post-processing is the principal reason the same code can be applied to seven geometrically and materially different tests without rewriting the solver.

The use of a jump function improves the physical bookkeeping. In the reduced formulation, phase expansion, segregation and thaw densification all enter as eigenstrain-like terms. In the enriched formulation, recoverable thermal/phase strain remains distributed, while persistent consolidation and creep are stored as explicit local displacement jumps. The decomposition is not only mathematical. It produces separate three-dimensional fields for axial displacement and inelastic jump and shows

Table 6
One-cycle FEAP jump–creep results. Creep jump is reported in micrometres; consolidation jump is the maximum absolute local bond jump. The enhanced model was not re-optimised against the endpoints.

Case	Hexp (mm)	HFEAP (mm)	Sexp (mm)	SFEAP (mm)	Heave APE (%)	Thaw APE (%)	max $\lvert\alpha^{(cr)}{}_n\rvert$ (μm)	max $\lvert\alpha^{c}{}_n\rvert$ (mm)
KF closed	3.780	3.840	2.155	2.146	1.60	0.40	0.231	0.0059
SK slurry	21.100	21.111	25.600	25.663	0.05	0.25	2.932	3.7634
PB slurry	16.300	17.540	14.200	15.456	7.61	8.84	2.719	0.5486
CKD slurry	16.400	17.625	19.400	20.511	7.47	5.72	2.758	1.6016
SK compacted	20.900	20.906	6.200	6.050	0.03	2.42	2.543	0.0000
PB compacted	21.700	22.488	17.700	17.786	3.63	0.49	2.071	0.4628
CKD compacted	22.900	24.008	19.900	19.079	4.84	4.13	2.304	0.4190

that the present short-duration tests are consolidation-dominated. Maximum creep jumps are below 3 μm, whereas consolidation jumps reach millimetres. A temperature-dependent creep law is nevertheless necessary for transfer to longer freezing periods or warmer frozen states because frozen-soil creep rates increase strongly near the melting range (Arenson and Springman, 2005; Xu et al., 2017; Cudmani et al., 2023).

The consolidation calculations provide a defensible bridge between laboratory data and lattice stiffness. SK slurry has the lowest C_v and $\Pi_c > 1$, consistent with slow dissipation and large thaw settlement. PB is highly compressible at 2 kPa, but its larger C_v permits faster redistribution. CKD has the largest C_v and k and a larger constrained modulus than PB. KF shows pronounced stress-dependent stiffening and a much larger apparent unloading modulus, which is consistent with a predominantly irreversible loading path. These quantities are sufficient to constrain normal lattice stiffness and consolidation capacity. They are not strength data. A conclusive shear-strength or failure prediction requires independent frozen and unfrozen triaxial/direct-shear/tensile tests; using the present oedometer and freeze–thaw endpoints to report cohesion or friction angle would be non-identifiable.

The stage-wise fields provide a conditional numerical interpretation of the closed/open contrast. In the KF calculation, the imposed external-wall temperature produces radial inward freezing and the no-flow tags prevent exchange of the reduced total-water variable across the specimen boundary. In the six open-column calculations, the cooled top and prescribed basal reservoir permit redistribution within the reduced transport law. These choices generate stronger predicted vertical water/ice gradients and larger calibrated heave. The pattern is consistent with classical distinctions between closed- and open-system frost action (Terzaghi et al., 1996; Konrad and Morgenstern, 1981; Konrad and Seto, 1994; Al-Hussaini, 2017), but it is not a unique mechanistic inference from the displacement data. The important demonstrated point is narrower: the code can impose the two documented boundary-value problems without changing its numerical architecture, whereas KF and PB should not be compared as if soil type were their only difference.

Initial state is equally important. SK slurry and compacted SK have the same mineral identity but similar heave and radically different thaw settlement. The model reproduces this by changing measured void ratio, density, water storage and consolidation capacity rather than changing the lattice topology. PB and CKD exhibit smaller but still material-state-dependent differences. Consequently, a single frost-susceptibility index cannot predict the complete cycle. Heave, thaw settlement, residual deformation and time-dependent consolidation must be evaluated separately.

The evidence has three explicitly separated levels. Verification is provided by the analytical heat, Stefan and compression benchmarks, the fixed-seed combined-resolution study and CPU-backend agreement. Calibration is demonstrated by the close first-cycle endpoint reproduction, with median APE 0.36%, using case-level parameters where complete thermal, hydraulic and mechanical data were unavailable. Validation is limited to the unfitted qualitative KF cycle-to-cycle reduction and plateau trend. The FEAP jump–creep rerun retains the calibrated coefficients and adds the local jump and creep physics without endpoint retuning; its median APE of 3.03% and maximum of 8.84% provide a cross-formulation stability check, not independent validation of a universal frozen-soil law. The 30.4% underprediction of the initial KF heave rate remains a useful discrepancy, pointing to limitations of the smooth homogeneous freezing curve, omitted apparatus heat capacity and unresolved discrete lensing.

Within this laboratory scope, the code is easy to deploy because all case differences are expressed in data rather than branches in the governing algorithm. A new case requires a geometry, initial state, boundary tags, schedule and parameter record. Preprocessing is automatic; the solver writes histories, stage snapshots, bond jumps, residuals and VTK files; and the same plotting functions produce 1D comparisons, 2D fields and revolved 3D atlases. Process-level parallelism gave a 3.25-fold speedup for seven independent cases with four CPU workers. The GPU path is also explicit and reproducible, but no device speedup is claimed because compatible hardware was unavailable. For larger meshes, benefit will require device-resident edge assembly, state update and preconditioning rather than transferring only the sparse system (Xue et al., 2023).

The FEAP template is a portability route, not evidence that the calculation was run in FEAP. The Python implementation follows the FEAP residual–tangent contract and supplies a Fortran user-element skeleton with the same history variables. This makes independent reproduction in FEAP feasible while keeping the executable reference code available in a language that could be run and verified in the present environment. A direct FEAP compilation and comparison should be included in future code-verification work.

The model remains reduced order. The total-water equation is conservative only within its bounded discrete storage/flux definition; it is not a Darcy–Richards flow law coupled to Biot effective stress, and it contains no explicit ice-lens nucleation or growth criterion. The pressure output is a cryogenic/storage proxy. Discrete ice lenses, crack nucleation, wall adfreezing, large deformation and material advection are not resolved. The three-dimensional plots are revolved axisymmetric visualisations, not independent three-dimensional meshes. Internal fields are therefore conditional model predictions constrained mainly by displacement endpoints and prescribed boundaries, not unique measurements or validated reconstructions. Stronger validation requires raw synchronized records, replicate tests, internal pore pressure, radial deformation/stress, salinity, soil-freezing characteristic curves, before/after permeability and multiaxial strength/creep tests.

For other frozen soils, the same architecture can be retained while replacing the data record and, where needed, the constitutive module. Clay-rich soils require measured unfrozen-water curves and broad phase transitions; silts require water-migration and lens criteria; saline soils require freezing-point depression; organic or ice-rich soils require compressible ice-rich and large-strain laws. Layering is introduced through nodal and bond-wise parameters. Open drainage must be represented by a hydraulic boundary, not by artificially increasing the heave coefficient. Fracture or major thaw collapse should be treated with embedded damage, phase-field, peridynamic, DEM or MPM extensions (Suh and Sun, 2022; Kebria and Na, 2024; Zheng et al., 2024; J. Yu et al., 2024; Li et al., 2024; Li and Yin, 2025). Thus, the present results demonstrate a convenient and transferable computational workflow for calibrated laboratory displacement assessment, but not universal field prediction or unique identification of water-migration mechanisms.

5. Conclusions

A source-grounded, axisymmetric Voronoi–Delaunay lattice model was developed for closed- and open-system laboratory freeze–thaw problems. The revised formulation adds explicit specimen geometry and staged initialization, a FEAP-compatible residual–tangent edge contract, Heaviside displacement-jump kinematics, separate consolidation and creep histories, and a bounded temperature- and ice-dependent Norton–Glen creep law. The same preprocessor and solver handle a closed, externally cooled KF cylinder and six open, top-down columns without changing the governing algorithm.

The thermal, phase and mechanical operators were verified against analytical radial conduction, Stefan-front and confined-compression problems with errors of 1.45%, 3.53% and 5.88%. Source consolidation data gave material-specific C_v, m_v, hydraulic conductivity and constrained-modulus constraints. The available records did not support independent shear or tensile strength calculation; strength parameters are therefore identified as priors rather than measurements.

The calibrated reduced model reproduced 14 first-cycle heave and thaw-settlement endpoints with median APE 0.36%. When the FEAP jump–creep enrichment was activated without endpoint re-optimisation, median and maximum errors were 3.03% and 8.84%.

Maximum creep jumps remained below 3 μm, while consolidation jumps reached 3.76 mm, indicating that, within the calibrated reduced model, the short tests are represented mainly by phase-change and thaw-consolidation terms rather than long-term creep. Stage-wise revolved fields illustrate the predicted contrast between radial closed-system and vertically forced open-system calculations, but these internal fields are not independently validated.

The code provides automated meshing, source-data presets, sparse CPU-direct and iterative solution, process-parallel case execution, optional GPU-CG with deterministic CPU fallback, stage scrolling and VTK export. Four CPU workers produced a measured 3.25-fold seven-case speedup. This evidence supports use of the lattice code as a rapid calibrated laboratory displacement-assessment and scenario-comparison tool. Further predictive development should add measured freezing characteristic and retention functions, full water/effective-stress coupling, direct FEAP compilation, multiaxial strength and creep calibration, explicit ice-lens or damage laws, large deformation and hardware-specific GPU benchmarking.

Declaration of generative AI and AI-assisted technologies in the manuscript preparation process

During the preparation of this work, the authors used OpenAI ChatGPT to assist with manuscript organization, language refinement, LaTeX preparation, and software drafting and debugging. The authors subsequently reviewed and edited the manuscript, verified the source data, equations, references, code and numerical outputs, and take full responsibility for the content of the article.

CRediT authorship contribution statement

Zarghaam Rizvi: Writing – review & editing, Writing – original draft, Visualization, Validation, Software, Resources, Methodology, Investigation, Formal analysis, Data curation, Conceptualization. **Mohammad Arsalan Khan:** Writing – review & editing, Visualization, Validation, Methodology, Investigation, Formal analysis, Data curation. **Frank Wuttke:** Writing – review & editing, Validation, Resources, Project administration, Funding acquisition.

Code availability

The submission archive contains the source code for preprocessing, coupled solution, analytical benchmarks, seven-case execution, constitutive material-point checks, CPU process-parallel benchmarking, optional GPU sparse solution, figure generation and VTK export. A permanent repository identifier should be assigned to the final frozen release before acceptance.

Funding

This research did not receive any specific grant from funding agencies in the public, commercial, or not-for-profit sectors.

Declaration of competing interest

The authors declare that they have no known competing financial interests or personal relationships that could have appeared to influence the work reported in this paper.

Acknowledgements

The authors thank Dr. Nina Keul for facilitating participation in the expedition aboard RV *Alkor* and access to the Kieler Förde samples, Dr.-Ing. Henok Hailemariam for laboratory-equipment support, and the technical staff who manufactured the modified apparatus.

Appendix A. Supplementary data

Supplementary data to this article can be found online at https://doi.org/10.1016/j.coldregions.2026.105164.

Data availability

The processed material database, experimental scalar targets, verification outputs, numerical result summaries and data used to generate the figures are included in the accompanying reproducibility package. The Kieler Förde source record and the Al-Hussaini thesis remain the primary experimental sources. Original machine-readable instrument streams were not available for every case; therefore, continuous laboratory histories were not reconstructed or fabricated.

References

Al-Hussaini, Osama Mahdi, 2017. Volume Change Behaviour of Some Geomaterials Under Combined Influence of Freeze–Thaw and Wet–Dry Cycles: An Experimental Investigation. PhD thesis. Cardiff University.

Andersland, Orlando B., Ladanyi, Branko, 2004. Frozen Ground Engineering, 2nd ed. Wiley, Hoboken.

Arenson, Lukas U., Springman, Sarah M., 2005. Mathematical descriptions for the behaviour of ice-rich frozen soils at temperatures close to 0 °c. Can. Geotech. J. 42 (2), 431–442. https://doi.org/10.1139/t04-109.

Bardenhagen, Scott G., Kober, Edward M., 2004. The generalized interpolation material point method. Comput. Model. Eng. Sci. 5 (6), 477–495. https://doi.org/10.3970/cmes.2004.005.477.

Benson, Craig H., Othman, Mohamed A., 1993. Hydraulic conductivity of compacted clay frozen and thawed in situ. J. Geotech. Eng. 119 (2), 276–294. https://doi.org/10.1061/(ASCE)0733-9410(1993)119:2(276).

Biot, Maurice A., 1941. General theory of three-dimensional consolidation. J. Appl. Phys. 12 (2), 155–164. https://doi.org/10.1063/1.1712886.

Bolander, John E., Saito, Shigehiko, 1998. Fracture analyses using spring networks with random geometry. Eng. Fract. Mech. 61 (5–6), 569–591. https://doi.org/10.1016/S0013-7944(98)00069-1.

Bolander, John E., Sukumar, N., 2005. Irregular lattice model for Quasistatic crack propagation. Phys. Rev. B 71, 094106. https://doi.org/10.1103/PhysRevB.71.094106.

Bourdin, Blaise, Francfort, Gilles A., Marigo, Jean-Jacques, 2000. Numerical experiments in revisited brittle fracture. J. Mech. Phys. Solids 48 (4), 797–826. https://doi.org/10.1016/S0022-5096(99)00028-9.

Brebbia, Carlos A., Telles, Jose C.F., Wrobel, Luiz C., 1984. Boundary Element Techniques: Theory and Applications in Engineering. Springer, Berlin.

Carslaw, Horatio S., Jaeger, John C., 1959. Conduction of Heat in Solids, 2nd ed. Oxford University Press, Oxford.

Chamberlain, Edwin J., 1981. Overconsolidation effects of ground freezing. Eng. Geol. 18, 97–110. https://doi.org/10.1016/0013-7952(81)90050-8.

Chamberlain, Edwin J., Gow, Anthony J., 1979. Effect of freezing and thawing on the permeability and structure of soils. Eng. Geol. 13, 73–92. https://doi.org/10.1016/0013-7952(79)90022-X.

Chang, Dan, Yan, Yihui, Liu, Jiankun, Xu, Anhua, et al., 2023. Micro-macroscopic mechanical behavior of frozen sand based on a large-scale direct shear test. Comput. Geotech. 159, 105484. https://doi.org/10.1016/j.compgeo.2023.105484.

Collins, Ian F., Houlsby, Guy T., 1997. Application of thermomechanical principles to the modelling of geotechnical materials. Proc. R. Soc. A 453, 1975–2001. https://doi.org/10.1098/rspa.1997.0107.

Crank, John, 1984. Free and Moving Boundary Problems. Clarendon Press, Oxford.

Cudmani, Roberto, Yan, Wei, Schindler, Ulrich, 2023. A Constitutive model for the simulation of temperature-, stress- and rate-dependent behaviour of Frozen Granular soils. Géotechnique 73 (12), 1043–1055. https://doi.org/10.1680/jgeot.21.00012.

Cundall, Peter A., Strack, Otto D.L., 1979. A discrete numerical model for granular assemblies. Geotechnique 29 (1), 47–65. https://doi.org/10.1680/geot.1979.29.1.47.

Dall'Amico, Mattia, Endrizzi, Stefano, Gruber, Stephan, Rigon, Riccardo, 2011. A robust and energy-conserving model of freezing variably-saturated soil. Cryosphere 5, 469–484. https://doi.org/10.5194/tc-5-469-2011.

Delaunay, Boris, 1934. Sur La Sphere Vide. Bull. Acad. Sci. URSS, Cl. Sci. Math. Nat. 6, 793–800.

Eigenbrod, Klaus D., 1996. Effects of cyclic freezing and thawing on volume changes and permeabilities of soft fine-grained soils. Can. Geotech. J. 33 (4), 529–537. https://doi.org/10.1139/t96-079-301.

Eigenbrod, Klaus D., Knutsson, Sven, Sheng, Daichao, 1996. Pore-water pressures in freezing and thawing fine-grained soils. J. Cold Reg. Eng. 10 (2), 77–92. https://doi.org/10.1061/(ASCE)0887-381X(1996)10:2(77).

Fredlund, Delwyn G., Xing, Anqing, 1994. Equations for the soil-water characteristic curve. Can. Geotech. J. 31 (4), 521–532. https://doi.org/10.1139/t94-061.

Gilpin, R.R., 1980. A model for the prediction of ice lensing and frost heave in soils. Water Resour. Res. 16 (5), 918–930. https://doi.org/10.1029/WR016i005p00918.

Grassl, Peter, 2009. A lattice approach to model flow in cracked concrete. Cem. Concr. Compos. 31 (7), 454–460. https://doi.org/10.1016/j.cemconcomp.2009.05.001.

Grassl, Peter, Bolander, John E., 2016. Three-dimensional network model for coupling of fracture and mass transport in Quasi-Brittle geomaterials. Materials 9 (9), 782. https://doi.org/10.3390/ma9090782.
Harlan, Richard L., 1973. Analysis of coupled heat-fluid transport in partially frozen soil. Water Resour. Res. 9 (5), 1314–1323. https://doi.org/10.1029/WR009i005p01314.
Harris, Charles R., Jarrod Millman, K., van der Walt, Stéfan J., et al., 2020. Array programming with NumPy. Nature 585, 357–362. https://doi.org/10.1038/s41586-020-2649-2.
Hendry, M.T., Onwude, L.U., Sego, D.C., 2016. A laboratory investigation of the frost heave susceptibility of fine-grained soil generated from abrasion of a diorite aggregate. Cold Reg. Sci. Technol. 123, 91–98. https://doi.org/10.1016/j.coldregions.2015.11.016.
Houlsby, Guy T., Puzrin, Alexander M., 2000. A thermomechanical framework for constitutive models for rate-independent dissipative materials. Int. J. Plast. 16 (9), 1017–1047. https://doi.org/10.1016/S0749-6419(99)00073-X.
Houlsby, Guy T., Puzrin, Alexander M., 2006. Principles of Hyperplasticity: An Approach to Plasticity Theory Based on Thermodynamic Principles. Springer, London. https://doi.org/10.1007/978-1-84628-240-9.
Hrennikoff, Alexander, 1941. Solution of problems of elasticity by the framework method. J. Appl. Mech. 8 (4), A169–A175.
Hunter, John D., 2007. Matplotlib: a 2D graphics environment. Comput. Sci. Eng. 9 (3), 90–95. https://doi.org/10.1109/MCSE.2007.55.
Hwang, Young Kwang, Jin, Suyeong, Hong, Jung Wuk, 2022. Fracture simulations using edge-based smoothed finite element method for isotropic damage model via delaunay/voronoi dual tessellations. Int. J. Damage Mech. 31 (3), 348–373. https://doi.org/10.1177/10567895211040549.
Kawai, Tadahiko, 1978. New discrete models and their application to seismic response analysis of structures. Nucl. Eng. Des. 48 (1), 207–229. https://doi.org/10.1016/0029-5493(78)90217-0.
Kebria, Mahyar Malekzade, Na, SeonHong, 2024. A coupled phase-field method and thermo-hydro-mechanics based framework for analyzing saturated ice-rich porous materials. Int. J. Numer. Anal. Methods Geomech. 48 (5), 1245–1277. https://doi.org/10.1002/nag.3685.
Kolymbas, Dimitrios, 1991. An Outline of Hypoplasticity. Arch. Appl. Mech. 61, 143–151. https://doi.org/10.1007/BF00788048.
Konrad, Jean-Marie, 1989. Effect of freeze–thaw cycles on the freezing characteristics of a clayey silt at various overconsolidation ratios. Can. Geotech. J. 26 (2), 217–226. https://doi.org/10.1139/t89-031.
Konrad, Jean-Marie, Lemieux, Nathalie, 2005. Influence of fines on frost heave characteristics of a well-graded base-course material. Can. Geotech. J. 42 (2), 515–527. https://doi.org/10.1139/t04-115.
Konrad, Jean-Marie, Morgenstern, Norbert R., 1981. The segregation potential of a freezing soil. Can. Geotech. J. 18 (4), 482–491. https://doi.org/10.1139/t81-059.
Konrad, Jean-Marie, Seto, Jon T.C., 1994. Frost heave characteristics of undisturbed sensitive champlain sea clay. Can. Geotech. J. 31 (2), 285–298.
Koopmans, Raymond W.R., Miller, Robert D., 1966. Soil freezing and soil water characteristic curves. Soil Sci. Soc. Am. J. 30 (6), 680–685. https://doi.org/10.2136/sssaj1966.03615995003000060011x.
Krzaczek, M., Nitka, M., Tejchman, J., 2023. A novel DEM-based pore-scale thermal-hydro-mechanical model for fractured non-saturated porous materials. Acta Geotech. 18, 2487–2512. https://doi.org/10.1007/s11440-022-01746-8.
Lai, Yuanming, Xu, Xiangtian, Yu, Wenbing, Qi, Jilin, 2014. An experimental investigation of the mechanical behavior and a hyperplastic constitutive model of frozen loess. Int. J. Eng. Sci. 84, 29–53. https://doi.org/10.1016/j.ijengsci.2014.06.011.
Li, Kaiqi, Yin, Zhen-Yu, 2025. State of the art of coupled thermo-hydro-mechanical-chemical modelling for frozen soils. Arch. Comput. Methods Eng. 32 (2), 1039–1096. https://doi.org/10.1007/s11831-024-10164-w.
Li, Kaiqi, Yin, Zhen-Yu, Qi, Jilin, et al., 2024. State-of-the-art constitutive modelling of frozen soils. Arch. Comput. Methods Eng. 31, 3801–3842. https://doi.org/10.1007/s11831-024-10102-w.
Liu, Qianqian, Cai, Guoqing, et al., 2024. Thermo-hydro-mechanical coupled model of unsaturated frozen soil considering frost heave and thaw settlement. Cold Reg. Sci. Technol. 217, 104026. https://doi.org/10.1016/j.coldregions.2023.104026.
Miehe, Christian, Hofacker, Martina, Welschinger, Fabian, 2010. A phase field model for rate-independent crack propagation: robust algorithmic implementation based on operator splits. Comput. Methods Appl. Mech. Eng. 199 (45–48), 2765–2778. https://doi.org/10.1016/j.cma.2010.04.011.
Miller, Robert D., 1972. Freezing and heaving of saturated and unsaturated soils. Highw. Res. Rec. 393, 1–11.
Morgenstern, Norbert R., Nixon, J.F., 1971. One-dimensional consolidation of thawing soils. Can. Geotech. J. 8 (4), 558–565. https://doi.org/10.1139/t71-057.
Niemunis, Andrzej, Herle, Igor, 1997. Hypoplastic model for cohesionless soils with elastic strain range. Mech. Cohesive-Frict. Mater. 2 (4), 279–299. https://doi.org/10.1002/(SICI)1099-1484(199710)2:4<279::AID-CFM29>3.0.CO;2-8.
Nikolic, Mijo, Ibrahimbegovic, Adnan, Miscevic, Predrag, 2016. Discrete element model for the analysis of fluid-saturated fractured poro-plastic medium based on sharp crack representation with embedded strong discontinuities. Comput. Methods Appl. Mech. Eng. 298, 407–427. https://doi.org/10.1016/j.cma.2015.10.009.
Nishimura, Soichiro, Gens, Antonio, Olivella, Sebastia, Jardine, Richard J., 2009. THM-coupled finite element analysis of frozen soil: formulation and application. Geotechnique 59 (3), 159–171. https://doi.org/10.1680/geot.2009.59.3.159.
Norouzi, Emad, Li, Biao, 2024. Finite element modeling of thermal-hydro-mechanical coupled processes in unsaturated freezing soils considering air-water capillary pressure and cryosuction. Int. J. Numer. Anal. Methods Geomech. 48 (11), 2944–2970. https://doi.org/10.1002/nag.3761.
Okuta, Ryosuke, Unno, Yuya, Nishino, Daisuke, Hido, Shohei, Crissman, Clayton, 2017. CuPy: a NumPy-compatible library for NVIDIA GPU calculations. In: Workshop on Machine Learning Systems. NeurIPS. https://doi.org/10.48550/arXiv.1712.05051.
O'Neill, Kevin, Miller, Robert D., 1985. Exploration of a rigid ice model of frost heave. Water Resour. Res. 21 (3), 281–296. https://doi.org/10.1029/WR021i003p00281.
Ostoja-Starzewski, Martin, 2002. Lattice models in micromechanics. Appl. Mech. Rev. 55 (1), 35–60. https://doi.org/10.1115/1.1432990.
Patankar, Suhas V., 1980. Numerical heat transfer and fluid flow. Hemisphere, Washington, DC.
Rempel, Alan W., 2007. Formation of ice lenses and frost heave. J. Geophys. Res. Earth Surf. 112, F02S21. https://doi.org/10.1029/2006JF000525.
Rizvi, Zarghaam, 2019. Lattice Element Method and its Application to Multiphysics Problems in Geomechanics. PhD thesis. Kiel University.
Schlangen, Erik, van Mier, Jan G.M., 1992. Experimental and numerical analysis of micromechanisms of fracture of cement-based composites. Cem. Concr. Compos. 14 (2), 105–118. https://doi.org/10.1016/0958-9465(92)90004-F.
Silling, Stewart A., 2000. Reformulation of elasticity theory for discontinuities and long-range forces. J. Mech. Phys. Solids 48 (1), 175–209. https://doi.org/10.1016/S0022-5096(99)00029-0.
Spaans, Egbert J.A., Baker, John M., 1996. The soil freezing characteristic: its measurement and similarity to the soil moisture characteristic. Soil Sci. Soc. Am. J. 60 (1), 13–19. https://doi.org/10.2136/sssaj1996.03615995006000010005x.
Stefan, Josef, 1891. Uber die theorie der eisbildung, insbesondere uber die eisbildung im polarmeere. Ann. Phys. 278, 269–286.
Suh, Hyeon Seok, Sun, WaiChing, 2022. Multi-phase-field microporomechanics model for simulating ice lens growth and thaw in frozen soil. Comput. Methods Appl. Mech. Eng. 394, 114901. https://doi.org/10.1016/j.cma.2022.114901.
Sulsky, Deborah, Chen, Zhen, Schreyer, Howard L., 1994. A particle method for history-dependent materials. Comput. Methods Appl. Mech. Eng. 118, 179–196. https://doi.org/10.1016/0045-7825(94)90112-0.
Taber, Stephen, 1930. The mechanics of frost heaving. J. Geol. 38 (4), 303–317. https://doi.org/10.1086/623720.
Taylor, Robert L., 2020. FEAP — A Finite Element Analysis Program: Theory Manual. Department of Civil; Environmental Engineering, University of California, Berkeley. https://projects.ce.berkeley.edu/feap/theory_86.pdf.
Terzaghi, Karl, Peck, Ralph B., Mesri, Gholamreza, 1996. Soil Mechanics in Engineering Practice, 3rd ed. Wiley, New York.
Thomas, Hywel R., Cleall, Peter, Li, Y.-C., Harris, C., Kern-Luetschg, M., 2009. Modelling of cryogenic processes in permafrost and seasonally frozen soils. Geotechnique 59 (3), 173–184. https://doi.org/10.1680/geot.2009.59.3.173.
van Genuchten, M.T., 1980. A closed-form equation for predicting the hydraulic conductivity of unsaturated soils. Soil Sci. Soc. Am. J. 44 (5), 892–898. https://doi.org/10.2136/sssaj1980.03615995004400050002x.
Viklander, Peter, 1998. Laboratory study of stone heave in till exposed to freezing and thawing. Cold Reg. Sci. Technol. 27 (2), 141–152. https://doi.org/10.1016/S0165-232X(98)00004-4.
Virtanen, Pauli, Gommers, Ralf, Oliphant, Travis E., et al., 2020. SciPy 1.0: fundamental algorithms for scientific computing in Python. Nat. Methods 17, 261–272. https://doi.org/10.1038/s41592-019-0686-2.
von Wolffersdorff, Peter-Andreas, 1996. A hypoplastic relation for granular materials with a predefined limit state surface. Mech. Cohesive-Frict. Mater. 1 (3), 251–271. https://doi.org/10.1002/(SICI)1099-1484(199607)1:3<251::AID-CFM13>3.0.CO;2-3.
Voronoi, Georgy, 1908. Nouvelles applications des Parametres Continus a la Theorie des Formes Quadratiques. J. Reine Angew. Math. 134, 198–287.
Wang, Decheng, Ma, Wei, Niu, Fujun, Chang, Xiaoxiao, Wen, Zhi, 2007. Effects of cyclic freezing and thawing on mechanical properties of Qinghai–Tibet clay. Cold Reg. Sci. Technol. 48 (1), 34–43. https://doi.org/10.1016/j.coldregions.2006.09.008.
Wong, L.C., Haug, M.D., 1991. Cyclical closed-system freeze–thaw permeability testing of soil liner and cover materials. Can. Geotech. J. 28 (6), 784–793. https://doi.org/10.1139/t91-095.
Wu, Yajun, Zhai, Encheng, Zhang, Xudong, 2021. A study on frost heave and thaw settlement of soil subjected to cyclic freeze–thaw conditions based on hydro-thermal-mechanical coupling analysis. Cold Reg. Sci. Technol. 188, 103296. https://doi.org/10.1016/j.coldregions.2021.103296.
Xu, Guofang, Wu, Wei, Qi, Jilin, 2016. Modeling the viscous behavior of frozen soil with hypoplasticity. Int. J. Numer. Anal. Methods Geomech. 40 (15), 2061–2075. https://doi.org/10.1002/nag.2516.
Xu, Guofang, Peng, Chong, Wu, Wei, Qi, Jilin, 2017. Combined constitutive model for creep and steady flow rate of frozen soil in an unconfined condition. Can. Geotech. J. 54 (7), 907–914. https://doi.org/10.1139/cgj-2016-0139.
Xue, Tianju, Liao, Shuheng, Gan, Zhengtao, Park, Chanwook, Xie, Xiaoyu, Liu, Wing Kam, Cao, Jian, 2023. JAX-FEM: a differentiable GPU-accelerated 3D finite element solver for automatic inverse design and mechanistic data science. Comput. Phys. Commun. 291, 108802. https://doi.org/10.1016/j.cpc.2023.108802.
Yoshioka, Keita, Sattari, Amir, Nest, Mathias, Günther, Ralf-Michael, Wuttke, Frank, Fischer, Thomas, Nagel, Thomas, 2022. Numerical models of pressure-driven fluid percolation in rock salt: nucleation and propagation of flow pathways under variable stress conditions. Environ. Earth Sci. 81, 139. https://doi.org/10.1007/s12665-022-10228-9.
Yu, Fan, Guo, Ping, Na, SeonHong, 2022. A framework for constructing elasto-plastic constitutive models for frozen and unfrozen soils. Int. J. Numer. Anal. Methods Geomech. 46 (2), 436–466. https://doi.org/10.1002/nag.3306.
Yu, Jidu, Zhao, Jidong, Zhao, Shiwei, Liang, Weijian, 2024. Thermo-Hydro-mechanical coupled material point method for modeling freezing and thawing of porous media.

Int. J. Numer. Anal. Methods Geomech. 48 (13), 3308–3349. https://doi.org/10.1002/nag.3794.

Zhang, Yao, Michalowski, Radoslaw L., 2015. Thermal-hydro-mechanical analysis of frost heave and thaw settlement. J. Geotech. Geoenviron. Eng. 141 (7), 04015027. https://doi.org/10.1061/(ASCE)GT.1943-5606.0001305.

Zhelnin, Mikhail, Kostina, Anastasia, Plekhov, Oleg, Panteleev, Ivan, Levin, Lev, 2022. Coupled thermo-hydro-mechanical modeling of frost heave and water migration in freezing soils. J. Rock Mech. Geotech. Eng. 14 (2), 537–552. https://doi.org/10.1016/j.jrmge.2021.09.004.

Zheng, Junwei, Wang, Jian, Lu, Yang, Gu, Xin, Pastor, Manuel, Tayyebi, Saeid Moussavi, Mu, Yanhu, Wang, Tian, 2024. Modelling the frost cracking behavior in clayey soils: a peridynamic approach. Comput. Geotech. 176, 106765. https://doi.org/10.1016/j.compgeo.2024.106765.

Zienkiewicz, O.C., Taylor, R.L., Zhu, J.Z., 2005. The Finite Element Method: Its Basis and Fundamentals, 6th ed. Elsevier, Oxford.